

279014
578

**ANALYSIS OF A SIX-COMPONENT, FLOW-THROUGH,
STRAIN-GAGE, FORCE BALANCE USED FOR HYPERSONIC WIND
TUNNEL MODELS WITH SCRAMJET EXHAUST FLOW SIMULATION**

by

MARC W. KNISKERN

A thesis submitted to the Graduate Faculty of
North Carolina State University
in partial fulfillment of the
requirements for the Degree of
Master of Science

Department of Mechanical and Aerospace Engineering

**Raleigh
1990**

(NASA-CR-186585) ANALYSIS OF A
SIX-COMPONENT, FLOW-THROUGH, STRAIN-GAGE,
FORCE BALANCE USED FOR HYPERSONIC WIND
TUNNEL MODELS WITH SCRAMJET EXHAUST FLOW
SIMULATION M.S. Thesis Final Report

N90-21775

Unclas
G3/09 0279014

ABSTRACT

KNISKERN, MARC W. Analysis of a Six-Component, Flow-Through, Strain-Gage, Force Balance Used for Hypersonic Wind Tunnel Models with Scramjet Exhaust Flow Simulation. (Under the direction of Dr. John N. Perkins)

The purpose of this investigation was to evaluate the thermal effects of simulant gas injection and aerodynamic heating at the model's surface on the measurements of a non-watercooled, flow-through balance. A stainless steel model of a hypersonic airbreathing-propulsion cruise missile concept (HAPCM-50) was used to evaluate this balance. The tests were conducted in the 20-inch Mach 6 wind tunnel at NASA Langley Research Center. The balance thermal effects were evaluated at freestream Reynolds numbers ranging from $5 \times 10^6/\text{ft}$ to $7 \times 10^6/\text{ft}$ and angles of attack between -3.5 deg and 5 deg at Mach 6. The injection gases considered in the tests included cold air, hot air, and a mixture of 50% Argon and 50% Freon-12. The stagnation temperatures of the cold air, hot air, and Ar-Fr₁₂ reached 111°F, 214°F, and 283°F, respectively within the balance. A bakelite sleeve was inserted into the inner tube of the balance to minimize the thermal effects of these injection gases. Throughout the tests, the normal force, side force, yaw moment, roll moment, and pitching moment balance measurements were unaffected by the balance thermal effects of the injection gases and the wind tunnel flow. However, the axial force (AF) measurement was significantly affected by balance heating. The average zero shifts in the AF measurements were 1.9%, 3.8%, and 5.9% for cold air, hot air, and Ar-Fr₁₂ injection, respectively. The AF measurements decreased throughout these tests which lasted from 70 to 110 seconds. During the cold air injection tests, the AF measurements were accurate (less than 1% shift in AF) up to at least ten seconds after the model was injected into the wind tunnel test section. For the hot air and Ar-Fr₁₂ tests, the AF measurements were accurate up to at least five seconds after model injection. Possibly, the AF shifts could have been reduced by calibrating the forward and aft sections of the axial force bridge circuit independently. Within the scope of this investigation, non-watercooled, flow-through balances were not suitable for scramjet exhaust flow simulation tests.

**ANALYSIS OF A SIX-COMPONENT, FLOW-THROUGH,
STRAIN-GAGE, FORCE BALANCE USED FOR HYPERSONIC WIND
TUNNEL MODELS WITH SCRAMJET EXHAUST FLOW SIMULATION**

by

MARC W. KNISKERN

A thesis submitted to the Graduate Faculty of
North Carolina State University
in partial fulfillment of the
requirements for the Degree of
Master of Science

Department of Mechanical and Aerospace Engineering

Raleigh
1990

Approved By:

Advisory Committee Chairman

ACKNOWLEDGEMENTS

The author would like to thank Larry Huebner and Bill Monta for their assistance throughout this research project. Also, the financial support of NASA Langley Research Center is greatly appreciated. This work was supported in part by NASA cooperative agreement number NCC1-129. Finally, I wish to thank Dr. John Perkins, Dr. Fred DeJarnette, and Dr. J. Danby for serving on my committee.

LIST OF TABLES

| TABLE | | Page |
|--------------|---------------------------------|-------------|
| 1 | Computational Solutions | 24 |
| 2 | Test Matrix | 25 |
| 3 | Balance 2042 Zero Shifts | 26 |
| 4 | Balance 2042 Axial Force Shifts | 27 |

LIST OF FIGURES

| Figure | | Page |
|--------|---|------|
| 1 | HAPCM-50 Internal Gas Injection. | 28 |
| 2 | Force Accounting for the HAPCM-50. | 29 |
| 3 | NASA Langley 20-Inch Mach 6 Wind Tunnel Schematic. | 30 |
| 4 | Inner Balance Tube for Balance 2042. | 31 |
| 5 | Outer Balance Tube for Balance 2042. | 32 |
| 6 | Annular Beams and Strain Gage Mounting in Balance 2042. | 33 |
| 7 | Balance 2042 Strain-Gage Circuit Diagrams and Thermocouple Locations. | 34 |
| 8 | Injection Gas System. | 35 |
| 9 | Computational Grid for Parabolized Navier-Stokes Solutions. | 36 |
| 10 | Computational Solution-Experimental Comparison for the Unpowered Configuration at -3.5 deg AOA with $Re=7 \times 10^6/\text{ft}$ and $M=6$. | 37 |
| 11 | Balance Temperature Time Histories for the Unpowered Configuration at 5 deg AOA with $Re=7 \times 10^6/\text{ft}$ and $M=6$. | 38 |
| 12 | Axial Force and Balance Temperature Time Histories for the Unpowered Configuration at 5 deg AOA with $Re=0.5 \times 10^6/\text{ft}$ and $M=6$. | 39 |
| 13 | Balance Temperature Time Histories for the Powered Configuration at 0 deg AOA with $Re=0.5 \times 10^6/\text{ft}$ and $M=6$. | 40 |
| 14 | Balance Temperature Time Histories for the Powered Configuration at 0 deg AOA with $Re=7 \times 10^6/\text{ft}$ and $M=6$. | 40 |
| 15 | Axial Force and Balance Temperature Time Histories for the Unpowered Configuration at 0 deg AOA with $Re=7 \times 10^6/\text{ft}$ and $M=6$. | 41 |
| 16 | Axial Force and Balance Temperature Time Histories for the Unpowered Configuration at 5 deg AOA with $Re=7 \times 10^6/\text{ft}$ and $M=6$. | 42 |
| 17 | Balance Temperature Time Histories for the Powered Configuration at 5 deg AOA, $Re=0.5 \times 10^6/\text{ft}$, and $M=6$ with Cold Air Injection. | 43 |
| 18 | Balance Temperature Time Histories for the Powered Configuration at 5 deg AOA, $Re=0.5 \times 10^6/\text{ft}$, and $M=6$ with Hot Air Injection. | 44 |
| 19 | Balance Temperature Time Histories for the Powered Configuration at 5 deg AOA, $Re=0.5 \times 10^6/\text{ft}$, and $M=6$ with Ar-Fr ₁₂ Injection. | 45 |

| | | |
|----|---|----|
| 20 | Axial Force and Balance Temperature Time Histories for the Powered Configuration at 0 deg AOA, $Re=7 \times 10^6/\text{ft}$ and $M=6$ with Cold Air Injection. | 46 |
| 21 | Axial Force and Balance Temperature Time Histories for the Powered Configuration at 0 deg AOA, $Re=7 \times 10^6/\text{ft}$ and $M=6$ with Hot Air Injection. | 47 |
| 22 | Axial Force and Balance Temperature Time Histories for the Powered Configuration at 0 deg AOA, $Re=7 \times 10^6/\text{ft}$ and $M=6$ with Ar-Fr ₁₂ Injection. | 48 |

NOMENCLATURE

| SYMBOL | DESCRIPTION |
|------------------|--|
| AF | axial force balance measurement |
| AOA | angle of attack |
| Ar | Argon |
| C_{ac} | computational axial force coefficient |
| C_{ae} | experimental axial force coefficient |
| C_{nc} | computational normal force coefficient |
| C_{ne} | experimental normal force coefficient |
| Fr ₁₂ | Freon-12 |
| NF | normal force balance measurement |
| PM | pitching moment balance measurement |
| P_o | tunnel stagnation pressure |
| P_{tj} | stagnation pressure of the injection gas within the plenum |
| Re | freestream Reynolds number |
| RM | roll moment balance measurement |
| SF | side force balance measurement |
| T1 | balance thermocouple temperature 1 |
| T2 | balance thermocouple temperature 2 |
| T3 | balance thermocouple temperature 3 |
| T4 | balance thermocouple temperature 4 |
| T5 | balance thermocouple temperature 5 |
| T6 | balance thermocouple temperature 6 |
| T7 | balance thermocouple temperature 7 |
| T8 | balance thermocouple temperature 8 |
| T_{tj} | total temperature of the injection gas within the plenum |
| T_o | tunnel total temperature |
| YM | yaw moment balance component |

TABLE OF CONTENTS

| | Page |
|---|------|
| LIST OF TABLES | iii |
| LIST OF FIGURES | iv |
| NOMECLATURE | vi |
| 1. INTRODUCTION | 1 |
| 2. EXPERIMENTAL APPARATUS | 3 |
| 2.1 Facility description | 3 |
| 2.2 Model and Force Balance..... | 3 |
| 2.3 Injection Gas System..... | 6 |
| 3. COMPUTATIONAL PROCEDURE | 6 |
| 3.1 Algorithm..... | 6 |
| 3.2 Grid development and Computational solution | 7 |
| 4. EXPERIMENTAL TEST PROCEDURE | 8 |
| 5. RESULTS..... | 9 |
| 5.1 Computational Solution Comparison | 9 |
| 5.2 Balance Thermal Effects Without Simulant Gas Injection..... | 10 |
| 5.3 Balance Thermal Effects With Simulant Gas Injection | 16 |
| 5.3.1 Injection Gas Balance Thermal Effects | 17 |
| 5.3.2 Combined Thermal Effects..... | 19 |
| 6. CONCLUSIONS..... | 22 |
| 7. REFERENCES | 23 |
| 8. TABLES | 24 |
| 9. FIGURES | 28 |

1 INTRODUCTION

Due to the current renewed interest in hypersonic vehicles such as the National Aero-Space plane, accuracy and suitability of hypersonic test methods have become important issues. Specifically, wind tunnel testing of complete configuration hypersonic vehicles with scramjet engine simulation has been investigated by NASA and Rockwell International. Scramjet engine simulation is essential to evaluating the aerodynamic performance of these vehicles, since their entire undersurface is devoted to the propulsion system. Basically, the interactive aerodynamic effects of the scramjet engine contribute significantly to the vehicle aerodynamic forces and moments. However, duplication of scramjet engine operation is not feasible for wind tunnel models, since the combustion process is not geometrically scalable. Also, the complexity of the scramjet engine combustor and the high temperature of scramjet engine exhaust prevent the use of scramjet engines in typical hypersonic wind tunnels. The dilemma posed by the need for simulating scramjet engine operation and the nonpracticality of scaling a scramjet combustor has led to the technique of injecting a substitute cold gas to simulate the scramjet exhaust¹. This scheme is acceptable for matching the desired pressure distribution over the nozzle, thus simulating the effects of the scramjet engine upon the vehicle aerodynamic forces and moments.

Under the direction of NASA, Rockwell International conducted a survey of candidate test methods potentially suitable for obtaining aerodynamic data on hypersonic wind tunnel models with scramjet exhaust flow simulation¹. The most effective method utilizes a non-watercooled, flow-through, strain-gage force balance which provides a passage for the simulant scramjet exhaust within the model. Following the guidelines of Rockwell's investigation, NASA engineers constructed this particular balance (balance 2042) using inner and outer concentric tubes. The inner tube provides a passage for the simulant scramjet exhaust which is injected into the model and exhausted through the engine nozzle, as illustrated in Figure 1. Since the balance is directly exposed to the elevated temperatures of the simulant gas, temperature sensitivity problems of flow through balances are a major concern. During calibration, the balance is heated uniformly to typical operating temperatures, so temperature gradients within the balance are not included in the calibration process. Typically, watercooling is used to suppress temperature gradients. However, geometric constraints prevent the use of watercooling for flow-through balances in small-scale hypersonic wind tunnels. Since flow-through balances are directly exposed to

the simulant gas, convective heat transfer from this gas will develop temperature gradients within the balance which may significantly affect the accuracy of the balance. The purpose of this investigation was to determine if accurate force and moment data can be obtained during hypersonic wind tunnel tests using a non-watercooled, flow-through balance. A stainless steel model of a hypersonic airbreathing-propulsion cruise missile concept (HAPCM-50) was used for evaluating balance 2042. This research was performed under the cooperative hypersonic program between North Carolina State University and NASA Langley Research Center. The tests were conducted in the 20-inch Mach 6 wind tunnel at NASA Langley.

During the tests, a mixture of 50% Argon and 50% Freon-12 by volume was used to simulate scramjet exhaust. At moderate temperatures, this substitute gas yields nozzle pressure distributions which are nearly identical to the pressure distributions of hydrogen/air combustion products². Since the simulant gas replaces the scramjet exhaust, the inlet airflow must bypass the combustor nozzle. Otherwise, the mixture of inlet airflow and simulant gas would have an unknown composition and expansion characteristics. To accommodate this problem, a fairing was attached to divert the air flow around the inlet. This method was more acceptable than using an operable inlet, since the model geometry could not accommodate the simultaneous ingestion of inlet airflow and ejection of simulant scramjet exhaust¹. Clearly, this fairing would modify the flowfield of an operating inlet. Therefore, to obtain the proper aerodynamic forces and moments for the complete configuration with an operating inlet, a modular design of the HAPCM-50 was necessary. Using a modular design, four configurations of the HAPCM-50 could be tested separately to determine the complete configuration aerodynamic forces/moments with the scramjet engine properly simulated (see Figure 2 for illustration). In addition to analyzing the internal heating effects of the simulant gas on the balance, the external aerodynamic heating can also have adverse effects upon the accuracy of a non-watercooled balance. Hence, the accuracy of the balance without simulant gas injection was also investigated.

In addition to the experimental analysis, a parabolized Navier-Stokes (PNS) code was used to approximate the aerodynamic forces and moments on the vehicle. These results are necessary to define a specific time span for which accurate balance measurements are obtained. The balance was expected to produce accurate measurements near the beginning of each test, since internal and external heating effects become more significant as a test progresses. This application of computational fluid dynamics is opposite to standard

practice, since typically computational results are compared with experimental results to verify the accuracy of the computational solutions.

2 EXPERIMENTAL APPARATUS

2.1 FACILITY DESCRIPTION

The tests were conducted in the NASA Langley 20-inch Mach 6 wind tunnel depicted in Figure 3. This is a blow down wind tunnel with adjustable second minimums which exhausts to either a combination 41 ft diameter and 60 ft diameter vacuum spheres, a 100 ft vacuum sphere, or to atmosphere through an annular injector. Dry air is supplied from a 600 psia reservoir with a storage capacity of 42,000 ft³ and heated to a maximum temperature of 1000°R by an electrical resistance heater. Air for this reservoir is transferred from either 3000 psia or 4250 psi tank fields. An activated alumina dryer provides a dewpoint temperature of 419°R at a pressure of 600 psia. The wind tunnel has a two-dimensional, fixed geometry, contoured nozzle which is 7.45 ft in length. The 20.5 in. by 20 in. test section is fitted with two 16 in. diameter quartz windows for schlieren observation. The maximum run time is 10 to 15 minutes using the 100 ft sphere, 1.5 minutes for the two smaller spheres, and 20 minutes with the injector. A detailed description of this tunnel is presented in reference 3.

The Mach 6 tunnel has upper and lower injection systems within the test section. The upper injection system was used to inject a pitot pressure probe, while the model was mounted on the lower injection system. The lower injection system includes a manually operated, remotely controlled, sting support system. Injection time of the model was approximately one second with a maximum acceleration of 2g for force tests.

2.2 MODEL AND BALANCE

A stainless steel model of a hypersonic airbreathing-propulsion cruise missile concept (HAPCM-50) was used for this investigation. The overall dimensions of the model were 26 in. by 6 in. by 6 in.. To simplify the computational analysis, the wing

and stabilizers were omitted. Since the model space could not accommodate the simultaneous ingestion of inlet flow and ejection of the simulant scramjet exhaust, a fairing was used to divert the flow around the inlet. The HAPCM-50 model was constructed using a modular design so that four model configurations could be tested separately. Two configurations of the HAPCM-50 were evaluated during this investigation. These configurations included an unpowered configuration which excluded the wing, stabilizers, fairing, and scramjet engine and a powered configuration which excluded the wing and stabilizers but included the engine and fairing.

Using the guidelines of the Hartill report¹, balance engineers at NASA Langley designed and constructed a six-component, non-watercooled, flow-through balance. This balance was constructed using inner and outer concentric tubes, as shown in Figures 4 and 5, respectively. The outer tube was machined near each end to form strain-gaged beams necessary for force measurement. This included two annular beams (see Figures 5 and 6) which were used to measure axial force and eight rectangular beams which measured the remaining balance components. The inner and outer balance tubes were attached at the ends of the outer tube beyond the strain-gaged beams. The model was attached to the "free-floating" section of the outer balance tube (see Figure 5) which translated relative to the inner tube when an axial load was applied. The axial force was measured by eight strain gages which were mounted on the surface of the two annular beams. These beams restrained the movement of the "free-floating" section of the outer balance tube when an axial force was imparted on the model. The inner tube provides a passage for the simulant gas which flows through the hollow sting, into the balance, and out through four circular tubes which are perpendicular to the incoming flow. Then, the gas is collected in the plenum of the model and directed through the scramjet engine nozzle. To reduce the thermal effects of the injection gas upon the balance, a bakelite sleeve was inserted into the inner balance tube.

Strain-gage bridge circuits were used in balance 2042 to measure the vehicle forces and moments. Specifically, wheatstone bridge circuits were used to measure the normal force (NF), side force (SF), yawing moment (YM), pitching moment (PM), and roll moment (RM) components. To improve balance measurement accuracy and to negate the interactions of other forces/moments, four active strain

gages were mounted on the top and bottom of two rectangular beams for each of the bridge circuits measuring these components. Since the voltage output of a wheatstone bridge is based upon a comparative measure of resistances within the circuit⁴, uniform temperature increases of the strain gages within a bridge or uniform thermal expansion of the beams supporting these gages will not affect the bridge output. Therefore, only temperature variations within a particular bridge structure will affect the measurement of this component. To obtain the normal force and pitching moment components, the measurements of bridges Normal-1 and Normal-2 (see Figure 7) were added and subtracted, respectively. Similarly, the side force and yawing moment components were obtained by adding and subtracting the measurements of Side-1 and Side-2, respectively. Due to the complexity of measuring axial force, a double bridge circuit consisting of eight active strain gages was used to measure axial force. As shown in Figure 6, these strain gages were mounted on the surface of the annular beams. In addition, to measure the temperature variations within balance 2042, eight thermocouples were mounted within the balance. Thermocouples 3, 4, 6, and 7 were placed on the annular beams (see Figure 7). The remaining thermocouples were positioned adjacent to the various strain-gage bridge circuits.

To reduce the thermal sensitivity of balance 2042, the balance was calibrated in an oven. During this calibration, balance 2042 was heated uniformly to 180°F. Then, the balance was compensated for drift in the voltage output of each bridge circuit by adding segments of temperature sensitive wire to the appropriate circuits. The drift was caused by slight variations in the resistivities of the strain gages within a particular circuit. Also, the balance sensitivity was re-evaluated at 180°F during the temperature calibration. The sensitivity of balance 2042 was 0.5% of full scale (maximum) load which was typical of most balances. As indicated by the sensitivity, the balance was unable to accurately measure forces and moments less than 0.5% of full scale. The full scale load for the six balance components are listed in the load chart of Figure 7. The balance sensitivity was unaffected by uniform temperature increases.

2.3 Injection Gas System

The gas storage, metering, and control system, as illustrated in Figure 8, supplied the simulant gas to a connection at the rear of the model. Basically, this system consisted of a heated 22 ft³ storage vessel, Freon and Argon pumps, gas bottle manifolds, and control valves necessary to operate the system. Prior to filling the storage vessel, a vacuum pump was used to evacuate the system. For the simulant gas tests, the storage tank contained approximately 220 lbs of a 50% Freon and 50% Argon mixture. This mixture was heated to 500°F with a final pressure of 1390 psia. During each test, a control panel was used to remotely control the pressure within the model plenum. Further details of the system are presented in reference 5.

3 COMPUTATIONAL PROCEDURE

3.1 ALGORITHM

The parabolized Navier-Stokes (PNS) equations are the governing equations in the computational algorithm. These equations are obtained from the full compressible Navier-Stokes equations by neglecting the streamwise diffusion terms. By neglecting these terms, the PNS equations become a mixed set of hyperbolic-parabolic equations in the streamwise direction provided certain conditions are satisfied. These equations are valid for high Reynolds number flowfields which are predominantly supersonic without streamwise separation. As a result, a single-pass space marching procedure can be used to obtain a solution. The computational technique of Newsome et al.⁶ was chosen for the flowfield solutions. This method is based upon the upwind/relaxation algorithms developed by Thomas and Walters⁷ and uses an implicit upwind, finite-volume scheme that is fully conservative and second-order accurate. In developing this scheme, modifications were included to allow for marching with local iterations on crossflow planes. Upwind difference methods properly model the physical behavior of flowfields which remain supersonic, since these solutions are independent of downstream information. However, when the Navier-Stokes equations are applicable, streamwise subsonic flow will exist, typically in the boundary layer. This subsonic flow leads to "departure" (exponentially growing)

solutions to the PNS equations. The streamwise pressure gradient introduces a downstream influence in subsonic regions which makes downstream spatial marching ill-posed. To accommodate this problem, the technique of Vigneron⁸ was used to suppress departure solutions by reducing the influence of the streamwise pressure gradient.

3.2 GRID DEVELOPMENT AND COMPUTATIONAL SOLUTION

Using an external transfinite interpolation technique⁹, a grid was developed for the unpowered configuration of the HAPCM-50. This grid consisted of 42 cross-flow planes with 65 circumferential points on the half plane and 60 points between the body and outer boundary. Also, to adequately resolve sharp gradients near the body, approximately one-third of the normal points were clustered within the boundary layer. The outer boundary of the grid was defined to provide adequate shock capturing. Figure 9 illustrates a typical grid.

A conical starting solution was used to obtain a converged solution at the first cross-sectional plane. The solution was considered converged after the residual was reduced by three orders of magnitude. The residual was defined as the norm of the discretized steady-state terms in the governing equations. Once a converged conical solution was established, a marching technique was used to obtain converged solutions for the remaining cross-flow planes. A complete solution required approximately 28 minutes of Cray-2 computer time. PNS solutions were obtained for the unpowered configuration which excludes the scramjet engine, fairing, wing, and stabilizers. A perfect gas with a specific heat ratio of 1.4 was assumed for these solutions, since the freestream stagnation temperatures of the tunnel ranged from 410°R to 475°R. At these temperatures, real gas effects will not be prominent in the flowfield; hence, the perfect gas assumption was valid. At low Reynolds numbers ($Re < 1 \times 10^6/ft$), the solutions were assumed fully laminar and the remaining solutions were considered turbulent. The normal and axial coefficients were computed for angles of attack between -3.5 deg and 5 deg and Reynolds numbers ranging from $0.5 \times 10^6/ft$ to $7 \times 10^6/ft$ at Mach 6 (see Table 1).

4 EXPERIMENTAL TEST PROCEDURE

The tests were conducted in the 20-inch Mach 6 wind tunnel at NASA Langley Research Center. The balance heating effects were evaluated over a tunnel stagnation pressure range of 30 psi to 475 psi and a stagnation temperature range of 410°R to 475°R. These conditions correspond to freestream Reynolds numbers ranging from $0.5 \times 10^6/\text{ft}$ to $7 \times 10^6/\text{ft}$. The test matrix in Table 2 provides a detailed description of the test conditions. For the powered configuration, three injection gases were tested in the model. These gases included cold air, hot air, and Ar-Fr₁₂. For the cold and hot air injection gas tests, the simulant gas storage vessel contained approximately 100 lbs of air at 1500 psia. The stagnation temperature of the cold and hot air were 200°F and 500°F, respectively. The injection gas flow rate was remotely-controlled by a control panel to maintain a plenum stagnation pressure of 20 psia.

During each test, the model was mounted within the wind tunnel test section on a sting support strut which was an integral part of the model injection system. The model was injected into the airstream after the tunnel was started to prevent possible damage to the force balance which could result from large transient loads caused by starting the tunnel with the model positioned within the test section. For the gas injection tests, the simulant gas injection began after the model was positioned within the test section. The stagnation temperature and stagnation pressure of the simulant injection gas was measured within the plenum of the scramjet engine. For each test, time histories of the balance temperatures, normal force, axial force, side force, yaw moment, roll moment, and pitching moment were monitored and recorded. In addition, the base pressures and chamber pressures of the model were measured using 20 psi and 50 psi transducers, respectively. These pressures were necessary to exclude the base and chamber pressure contributions to the vehicle forces and moments. This procedure was typical of wind tunnel force and moment tests.

5 RESULTS

5.1 COMPUTATIONAL SOLUTION COMPARISON

A Parabolized Navier-Stokes code was used to approximate the aerodynamic forces and moments on the unpowered configuration of the HAPCM-50. These computational results were compared to time histories of the normal force (NF) and axial force (AF) balance measurements for Reynolds number ranging from $0.5 \times 10^6/\text{ft}$ to $7 \times 10^6/\text{ft}$ and for 5, 0, and -3.5 deg AOA. The purpose of this comparison was to define a specific time during the tests for which the balance measurements were most accurate. The NF and AF balance measurements were the only components necessary for this comparison since the bridge circuit measuring NF was in close proximity to the bridge circuits measuring the other balance components. So, balance temperature variations which affect the normal force measurement should similarly affect the side force (SF), roll moment (RM), pitching moment (PM), and yawing moment (YM) balance measurements. For example, the bridge circuits measuring SF, YM, and RM were located adjacent to bridge circuits Normal-1 and Normal-2 (see Figure 8) which measure the normal force and pitching moment. Hence, temperature gradients within the balance affecting NF measurements should similarly affect the SF, YM, and RM measurements. The balance was expected to yield most accurate measurements at the beginning of each run, since the balance thermal effects become more pronounced as a test progresses.

Throughout the unpowered configuration tests, the normal force balance measurements were unaffected by temperature variations within the balance resulting from aerodynamic heating at the surface of the model. During these tests, this balance component did not vary more than the normal sensitivity (0.5 lbs) of the balance. Hence, the time histories of the normal force balance measurement could not be used to define a specific time for which the balance measurements were most accurate. In Table 1, the experimental normal force coefficient (C_{ne}) measured five seconds after model injection was compared to the computational value (C_{nc}). The C_{ne} measurement immediately after model injection was not considered for this comparison since the vibrations of the model, sting, and balance after injection may affect the balance measurements. In general, the percent difference between C_{ne} and C_{nc} was less than 5.5%. However, the percent difference increased dramatically to

51.5% for 0 deg AOA. At 0 deg AOA, the normal force ranged from 0.2 lbs to 0.8 lbs; therefore, the poor comparison between C_{ne} and C_{nc} at this AOA was attributed to the balance sensitivity. Clearly, the balance was unable to accurately measure normal forces near 0.5 lbs (0.5% of the full scale normal force). Since the normal force measurements were unaffected by balance thermal effects during the unpowered configuration tests, the axial force measurements were used to establish the time at which most accurate balance measurements were obtained.

Unlike the normal force balance measurements, the axial force measurements were affected by aerodynamic heating at the model's surface. However, a vast majority of these runs were inconclusive, since either the axial component did not vary significantly during the test or the computational and experimental coefficients did not compare well enough to draw any direct conclusions. For example, at Reynolds numbers less than $1 \times 10^6/\text{ft}$, the axial force measurement did not vary beyond the balance sensitivity (0.11lbs) since the aerodynamic heating was apparently insignificant. However, for $Re > 1 \times 10^6/\text{ft}$ the balance thermal effects were significant. But, for a majority of these tests, the experimental axial force coefficient (C_{ae}) and the computational axial force coefficient (C_{ac}) compared poorly throughout each test. As shown in Table 1, the percent difference between C_{ac} and C_{ae} (measured five seconds after injection) varied from 3.2% to 65.8%. Since the maximum variation in C_{ae} during each of these tests was 4.2%, then the computational solutions where the percent difference between C_{ac} and C_{ae} (measured five seconds after injection) was significantly greater than 4.2% were not suitable for determining the time at which the axial force measurement was most accurate. Therefore, the only test suitable for this comparison was at -3.5 deg AOA and $Re = 7 \times 10^6/\text{ft}$ (see Table 1). During this particular test, the most accurate balance measurement of the axial force component occurred at the beginning of the test (see Figure 10). Conceivably, the accuracy of the balance diminished as the aerodynamic heating produced temperature gradients within the balance. These temperature gradients were apparent in the time histories of various balance temperatures which are presented in Figure 11. As expected, the most accurate balance measurements were obtained at the beginning of each test, and the accuracy of these measurements diminished as the balance was heated.

5.2 BALANCE THERMAL EFFECTS WITHOUT SIMULANT GAS INJECTION

To obtain the complete configuration aerodynamic forces and moments with the scramjet engines properly simulated, balance 2042 must be used to measure the forces and moments with and without simulant gas injection (see Figure 2). Without balance watercooling, the aerodynamic heating at the surface of the model may significantly affect the balance measurements. Hence, the balance thermal effects due to aerodynamic heating were evaluated for two configurations of the HAPCM-50. These configurations included the unpowered configuration and the powered configuration without simulant gas injection. Typically, zero shifts in balance components are used in hypersonic wind tunnel tests to indicate the variation in balance measurements during a test which result from balance heating. The zero shift in a balance component is the difference between the wind-off balance measurements before model injection and after model retraction with the tunnel at atmospheric pressure. In general, the zero shifts should indicate the accuracy of the six balance measurements during a particular test. To correlate zero shifts in the balance measurements with balance temperatures, time histories of various balance temperatures and three balance measurements were evaluated for various Reynolds numbers and angles of attack. As shown in Figure 7, thermocouples five and eight were located adjacent to the axial component strain-gage bridge and thermocouples one and two were adjacent to the side force, roll moment, and normal force balance component strain-gage bridges. Thermocouples three, four, six, and eight were mounted on the annular beams. These thermocouples should also describe the heat transfer from the model to the balance.

To understand the thermal effects of external aerodynamic heating upon the balance measurements, a qualitative analysis of heat transfer within the model and balance was necessary. Basically, the aerodynamic heating at the model's surface conducted through the surface of the model and entered the balance primarily through the balance lands (see Figure 6). Upon entering the balance, the heat was trapped by the axial web structure (see Figure 5). This web included an annular beam and four one-sixteenth inch rectangular beams connecting the ends of the outer tube to the center of the balance. The narrow passages of these beams effectively trap the heat entering through the lands. As a result, the temperatures within the center of the outer tube increased significantly for the high pressure runs ($Re=7 \times 10^6/\text{ft}$), as illustrated by

the time histories of T5 and T8 in Figures 11 and 14. Due to the web structure, the heat transfer rate was significantly reduced within the forward and aft ends of the balance. Only moderate temperature increases occurred in the ends of the balance. In general, the temperature increase within the ends of the outer balance tube was 70% less than the temperature increase in the vicinity of the balance lands, as demonstrated by T1 and T2 in Figures 11 and 14. Therefore, strain gage bridges used for force measurement which were closest to the balance lands should be most affected by aerodynamic heating at the model's surface.

For the unpowered tests, the NF, SF, YM, PM, and RM balance measurements were unaffected by aerodynamic heating. In general, the maximum zero shift of these measurements was 0.5%. Since the balance sensitivity was 0.5% of full scale, these zero shifts were negligible. Conceivably, these balance measurements were unaffected by the aerodynamic heating at the model's surface due to the location and structure of their respective strain-gage bridges. These bridges were situated at the ends of the outer balance tube. Hence, they were isolated from the aerodynamic heating. The temperature increase for the highest aerodynamic heating ($Re=7 \times 10^6/ft$) in the vicinity of these bridges (T1 and T2) was negligible compared to temperatures in the vicinity of the lands. The maximum temperature increase in T1 and T2 were $11^\circ F$ and $1^\circ F$, respectively. However, in the vicinity of the balance lands the maximum temperature rise was $35^\circ F$. Since the strain gages in each of these bridge circuits were mounted circumferentially at a given cross-sectional plane of the balance, only circumferential temperature gradients will affect these balance measurements. Unfortunately, only one thermocouple was placed at the forward and aft locations of these bridges; so, the circumferential temperature gradients could not be measured. Although the normal force and pitching moment measurements required outputs from two bridges located at opposite ends of the balance (Normal-1 and Normal-2 in Figure 7), these bridge measurements were independent of one another; therefore, axial temperature gradients within the balance will not affect these measurements. Similarly, axial temperature gradients will not affect the side force and yawing moment measurements. In conclusion, the NF, SF, YM, PM, and RM balance measurements were unaffected by the aerodynamic heating at the model's surface due to the isolation of their respective bridge circuits from the aerodynamic heating.

Ideally, the axial force measurements of balance 2042 should be unaffected by axial temperature variations. The "free floating" design of the outer balance tube and the structure of the axial component bridge circuit should minimize the sensitivity of the axial force measurements to axial temperature variations. The double bridge circuit measuring axial force included eight strain gages mounted on two annular beams (see Figures 6 and 7). The two sections of this circuit are mounted on the forward and aft annular beams. This circuit electrically averages the resistances of the strain gages experiencing tensile strains and averages the gages experiencing compressive strains. For example, when a positive axial load is applied to the balance, strain gages A1, A3, A5, and A7 (see Figure 7) experience tensile strains, and the remaining gages are compressed. Similar to the wheatstone bridge, this double bridge circuit uses a comparative measure of the resistances within the circuit to obtain the voltage output. Hence, provided the temperature of each annular beam increases uniformly, the voltage output of the double bridge circuit will be unaffected by thermal expansion of the annular beams and changes in the resistances of the strain gages within the double bridge circuit resulting from increasing temperatures. Due to the "free-floating" design of the outer balance tube, nonuniform axial thermal expansion, resulting from axial temperature variations, will not affect the axial force measurements if balance 2042 was ideally constructed. For example, aerodynamic heating causes the center of the outer balance tube to thermally expand while the inner balance tube and the ends of the outer balance tube remain isolated from the aerodynamic heating due to the web structure within the outer balance tube. Since the "free-floating" section of the outer balance tube remains in static equilibrium, the axial force experienced by the two annular beams due to thermal expansion will be equal in magnitude and opposite in direction. Provided the balance engineers designed the two annular beams with the same geometry, material properties, and strain gage locations, the resistance measurements of the forward and aft sections of the double bridge circuit will be equal and opposite; therefore, the voltage output of this circuit will be unaffected by axial thermal expansion. However, the geometry of the annular beams are only as accurate as the tolerances of the balance design. Specifically, the tolerance and thickness of the annular beams were ± 0.0005 in. and 0.0253 in., respectively. The strain at the surface of an annular beam is inversely proportional to the moment of inertia about the bending axis. For the worst possible scenario where the thicknesses of annular beams are $0.0253+0.0005$ in. and $0.0253-0.0005$ in., the moment of inertia's of these beams about the bending axis would differ by 11%. So, the strains at the surfaces of the

two annular beams could differ by as much as 11%. As a result, the axial loads caused by axial thermal expansion of the balance may not cancel within the double bridge circuit. Two improvements could have been incorporated to eliminate possible sensitivity of balance 2042 to axial temperature gradients. Either stricter tolerances could have been applied to the machining of the annular beams or an additional step could have been added to the calibration process. The simpler and equally effective alternative would be to include an additional step in the calibration of balance 2042. In this calibration step, the voltage outputs of the forward and aft sections of the double bridge circuit would be measured separately when an axial load was applied. Essentially, this would indicate if the magnitude of the strains at the surface of both annular beams were equal. Then, compensation in the form of resistive wire would be added to the circuit with the lower output so the circuits would have the same sensitivity. As a result, the axial forces imparted on the two annular beams resulting from axial thermal expansion will not affect the axial force measurement of balance 2042.

Overall the axial force measurements were significantly affected by aerodynamic heating at the model's surface. Zero shifts in the axial component varied from .6% to 4.0% for the low pressure runs ($Re < 4 \times 10^6/ft$). For the high pressure runs ($Re = 7 \times 10^6/ft$), these shifts ranged from 2.5% to 11.5% (see Table 3). Typically, zero shifts are representative of the variation in balance measurements during a test. However, in a few instances, the zero shifts in the axial components measurements of balance 2042 were not representative of the axial force measurements during the run. This was partly due to the time which transpired between model retraction from the test section and pumping the tunnel back to atmospheric pressure. This additional time allowed the heat to redistribute within the model and balance, thus affecting the zero shifts in the axial component which were measured after the tunnel reached atmospheric pressure. Hence, to accurately define the balance thermal effects on the axial force measurements during the tests, the shift in axial force which occurred between the time of model injection and retraction for each test was tabulated in Table 4. However, the axial force measurement immediately after model injection was not used to obtain these shifts since the vibrations of the model, sting, and balance may affect the balance measurements. Instead, the axial force measurement five seconds after injection was used to define the axial force shift during the run. During the low pressure tests, the axial force shift ranged from 0.3% to 1.7%, and for the

high pressure runs this shift varied from 1.8% to 4.2%. In general, as the freestream Reynolds number increased from $0.5 \times 10^6/\text{ft}$ to $7 \times 10^6/\text{ft}$ (P_o increased from 30 psia to 475 psia) the aerodynamic heating at the model's surface increased. The aerodynamic heating for $Re < 1 \times 10^6/\text{ft}$ had a negligible effect upon the axial force measurements. The balance temperatures did not increase more than 2°F , and the axial force shifts were less than the balance sensitivity. As illustrated in Figures 12 and 13, the balance temperatures were essentially constant for $Re=0.5 \times 10^6/\text{ft}$. However, for $Re=7 \times 10^6/\text{ft}$ the aerodynamic heating significantly affected the axial force measurements. As shown in Figures 14, 15, and 16, the balance temperatures adjacent to the balance lands (T5 and T8) increased by $20\text{-}30^\circ\text{F}$. The corresponding axial force measurements for the unpowered configuration at 0 and 5 deg AOA shifted by 4.2% and 2.8%, respectively (see Figures 15 and 16). For all the runs without gas injection, the axial force measurement decreased throughout the tests (see Table 4). For balance 2042, a 1% shift in the force and moment measurements was considered acceptable. This was the maximum acceptable shift because the measurement errors could magnify four-fold, since the forces/moments of four configurations must be summed to obtain the complete configuration aerodynamic forces/moments. Therefore, the axial force measurements of balance 2042 for $Re \leq 1 \times 10^6/\text{ft}$ were acceptable throughout the duration (approximately 80 secs) of these tests. However, this measurement was not acceptable throughout the runs where $Re > 1 \times 10^6/\text{ft}$ which lasted up to 110 seconds. So, unlike the other five balance components, the axial force measurement of balance 2042 was significantly affected by aerodynamic heating at the surface of the HAPCM-50.

The combined effects of axial bridge location and structure resulted in thermal sensitivity of the axial component. The strain gage bridge circuits of this component were mounted in the annular beams which were the closest force measuring structures to the balance lands. This region of the balance was subjected to the highest heat transfer rates since the balance lands were the primary path of heat conduction into the balance. Conceivably, both thermal expansion of the outer tube and circumferential temperature variations within the annular beams caused axial force shifts. For the high pressure runs, the temperature in the "free floating" section of the outer balance tube was $15\text{-}20^\circ\text{F}$ higher than the rest of the balance near the end of the runs. The thermal expansion of this section of the balance produced equal and opposite axial forces on the two annular beams used to measure axial force. Possibly,

the strains within these two sections of the axial bridge circuit did not cancel which would affect the axial force measurements. As the test progressed, the thermal expansion of the "free-floating" section increased with temperature (T5 and T8 indicated the temperature of this section). As a result, the axial force shift (see Figures 15 and 16) may have increased during the test due to this expansion. Also, the temperature variations within the forward annular beam increased throughout the tests, as illustrated by T3 and T4 in Figures 15 and 16. At the end of the high pressure tests, an 8°F temperature variation existed within this annular beam. As a result, the thermal expansion of this beam was not uniform. Since the bridge circuit can only compensate for uniform changes in the resistances of strain gages within each of the two sections of the axial double bridge circuit, the temperature variations within the forward annular beam contributed to the shift in axial force measurement. Also, since the annular beams were not heated uniformly, circumferential temperature variations existed in the the "free floating" section of the outer balance tube. Due to these temperature variations, the thermal expansions of the 1/16 inch rectangular beams were not identical. This would also contribute to axial force shifts by deflecting the annular beams. In conclusion, the axial force measurements of balance 2042 were significantly affected by circumferential temperature variations in the vicinity of the annular beams and possibly by thermal expansion of the "free-floating" section of the outer balance tube.

In typical force and moment tests without simulant gas injection, the balances were watercooled; hence, no restrictions applied to the length of the these tests since balance thermal effects were not a concern. Due to geometric constraints of flow-through balances, balance 2042 was not watercooled. As a result, balance thermal effects restrict the allowable length of flow-through balance tests. For the hypersonic test method of the HAPCM-50, the balance measurements were considered accurate up to a shift of 1% (of full scale). Since the axial force shift increased as each run progressed, the time span for accurate axial force measurements at the beginning of each test could be obtained. Based upon a 1% shift, the axial force measurements were accurate throughout the low tunnel pressure tests where $Re \leq 1 \times 10^6/\text{ft}$. However, for the remaining low pressure runs the axial force balance measurements were accurate within 30 seconds after model injection. The balance temperatures for these tests began increasing 20-25 seconds after injection. The more pronounced aerodynamic heating of the high pressure runs ($Re = 7 \times 10^6/\text{ft}$) caused the balance

temperatures to rise 10 seconds after model injection. As a result, the axial force measurements were only accurate up to 20 seconds after injection.

5.3 BALANCE THERMAL EFFECTS WITH SIMULANT GAS INJECTION

The main objective of this investigation was to evaluate the accuracy of balance 2042 during simulant gas injection tests. Three injection gases including cold air, hot air, and a 50% Ar/50% Fr₁₂ mixture were tested in the powered configuration of the HAPCM-50. Although the Ar-Fr₁₂ demonstrated nearly identical expansion characteristics to the hydrogen/air combustion products typical of scramjet engines, injection of cold air and hot air was necessary to consider the balance thermal effects of injection gases at different temperatures. The temperature of the Ar-Fr₁₂ mixture could not be reduced without the possibility of liquefaction during nozzle expansion. Balance thermal effects with cold air, hot air, and Ar-Fr₁₂ injection were evaluated for freestream Reynolds numbers of $.5 \times 10^6/\text{ft}$ and $7 \times 10^6/\text{ft}$ at 0 deg and 5 deg AOA, as shown in the test matrix (Table 2).

5.3.1 Injection Gas Balance Thermal Effects

The low tunnel pressure ($Re = .5 \times 10^6/\text{ft}$) gas injection tests were used to understand the heat transfer from the injection gas to the balance. These tests were indicative of the balance thermal effects of only the injection gas, since the aerodynamic heating was negligible. The cold air, hot air, and Ar-Fr₁₂ injection gas reached total temperatures of 96, 196, and 227°F, respectively within the balance. The total temperature (T_t) increased throughout each test (see Figure 17, 18, and 19) as a result of the increasing temperatures of the piping system which connected the injection gas storage tank to the model. As the temperature of these pipes increased the heat transfer rate from the injection gas to the surroundings decreased; thus, increasing the total temperature of the injection gas within the plenum of the model. Clearly, for an adiabatic piping system, the total temperatures of the injection gases would be identical to the storage tank temperatures which were 200, 500, and 500°F for the cold air, hot air, and Ar-Fr₁₂, respectively. Although the bakelite sleeve insulated the inner balance tube, the inner tube was dramatically heated by the injection gases, especially by the

hot air and Ar-Fr₁₂ (see Figures 17, 18, and 19). The heat within this tube conducted into the outer balance tube primarily through the attachment of these tubes at the aft end of balance 2042, as exemplified by the dramatic increase in T2 in Figures 17, 18, and 19. Unlike the aft end of balance 2042, the forward section of this balance was isolated from the thermal effects of the injection gas. This was expected since the injection gas exited the balance through four cylindrical tubes which were located between the balance lands (see Figure 6). So, the forward section of the balance was not exposed to the high temperatures of these gases. In general, the temperature rise within this region was one third of the temperature rise within the aft end of the balance (see T2 and T1 in Figures 17, 18, and 19).

The NF, SF, YM, RM, and PM balance measurements were unaffected by the balance thermal effects of simulant gas injection. In general, the zero shifts of these measurements which were indicative of the shifts during the runs did not exceed the balance sensitivity (see Table 3). Conceivably, the heat transfer from the injection gases had a negligible effect upon these balance measurements for two reasons: 1) the strain gage bridge structures at the front of the balance (Normal-1 and Side-1 in Figure 7) were isolated from the injection gas thermal effects, and 2) the convective heat transfer from the injection gas was symmetrical about the centerline of the inner balance tube in the vicinity of the strain gage bridge structures located in the aft section (Normal-2, Side-2, and Roll in Figure 7) of balance 2042. Since the injection gas exited the balance through four circular tubes located between the balance lands, the strain gage bridges in the forward section of the outer balance tube were isolated from the thermal effects of the high temperature injection gases. The temperature (T1) of the strain gage bridges at the front of the balance (Normal-1 and Side-1) increased by 4.3°F and 16°F for the cold air and hot air injection tests, respectively. Unfortunately, the thermocouple measuring T1 was not functional for the Ar-Fr₁₂ tests. As illustrated by Figures 17, 18, and 19, the temperature increase at the front of the balance (T1) was negligible in comparison to the aft section of the balance (T2). The heat from the inner balance tube conducted into the outer balance tube primarily through the attachment of the inner and outer tubes at the aft end of the balance. The strain-gaged beams measuring RM, S2, and N2 were adjacent to this attachment (see Figure 7). Hence, the temperature of these beams and their corresponding bridge circuits increased dramatically in comparison to the rest of the outer balance tube. As illustrated Figure in 19, the temperature (T2) increased by as much as 65°F for the

injection gas tests. Although the temperatures of these bridges increased dramatically, the balance measurements of SF, NF, RM, PM, and YM were unaffected since the temperatures of these bridges increased uniformly. Aforementioned, uniform increases in temperatures within a bridge will not affect the bridge output. The uniformity in balance temperatures at cross-sections in the aft section of the outer balance tube was illustrated by the temperatures within the aft annular beam (see T6 and T7 in Figures 17, 18, and 19). The maximum temperature difference within this beam for the cold air, hot air, and Ar-Fr₁₂ tests was 3.4°F. Symmetry in the temperatures within the aft section of the balance was expected, since the inner balance tube was merely a circular cylinder. Therefore, provided symmetrical pipe flow was established within this tube, the convective heat transfer rates from the injection gases will be symmetrical about the centerline. Since the outer balance tube was symmetrical about the centerline, the temperatures within this tube will be symmetrical for symmetrical heat transfer.

Unlike the other balance components, the axial force measurements were significantly affected by the balance heating of the three injection gases. For the low tunnel pressure runs, the average axial force zero shifts for the cold air, hot air, and Ar-Fr₁₂ tests were 1.3%, 3.4%, and 4.9%, respectively. For the hot air and Ar-Fr₁₂ injection tests, the axial force zero shifts increased dramatically, in comparison to the shifts for cold air injection, primarily due to the increase in total temperature of these gases which were 100°F and 150°F higher than the cold air total temperature, respectively. Since the temperatures within the forward and aft annular beams were essentially uniform for the low pressure ($Re = 0.5 \times 10^6/ft$) injection gas tests, the balance measurements were primarily affected by thermal expansion of the inner and outer balance tubes. As shown in Figures 17, 18, and 19, the temperature increases in the forward (T3 and T4) and aft (T6 and T7) annular beams were essentially uniform which will not affect axial force measurement. Since the inner balance tube was exposed to the heat transfer from the injection gas, this tube should thermally expand more than the outer balance tube. So, the annular beams in the outer balance tube experienced additional axial forces due to inner tube thermal expansion. Conceivably, the strains within the annular beams resulting from thermal expansion of the inner tube did not cancel within the double bridge circuit causing axial force shift. In general, the balance heating due to the hot air and Ar-Fr₁₂ injection gases was more pronounced than the heating caused by the tunnel flow. For the hot air and

Ar-Fr₁₂ injection gases, the balance temperatures began increasing 5 seconds after model injection. Whereas, the balance temperatures began increasing 10 seconds after model injection for the high tunnel pressure tests without gas injection. The more pronounced balance heating caused by the injection gases was expected, since the balance was directly exposed to the high temperatures of the hot air and Ar-Fr₁₂, whereas the aerodynamic heating at the surface of the model must conduct through the stainless steel model before affecting the balance.

5.3.2 Combined Balance Thermal Effects of Gas Injection and Aerodynamic Heating

The PM, YM, RM, NF, and SF balance measurements were unaffected by the combined thermal effects of tunnel flow and simulant gas injection. In general, the axial force zero shifts for the high tunnel pressure ($Re = 7 \times 10^6/ft$) gas injection tests did not exceed the balance sensitivity (see Table 3). However, the axial force measurements were significantly affected by the combined thermal effects of tunnel flow and gas injection. The average axial force zero shifts for the high pressure runs with cold air, hot air, and Ar-Fr₁₂ injection were 2.5%, 4.2%, and 7.0%, respectively. As expected, the balance thermal effects due to aerodynamic heating at the model's surface for the high tunnel pressure injection gas tests caused an increase in the axial force zero shifts relative to the low pressure injection gas tests. As illustrated by T6 and T7 in Figures 17, 18, and 19, temperature variations were prevalent within the annular beams which was not the case for the low tunnel pressure injection tests. Aforementioned, the temperature variations within the annular beams was a direct result of aerodynamic heating at the model's surface. At the end of the high tunnel pressure tests, the temperature variations within the aft annular beam were 5, 9, and 11°F for the cold air, hot air, and Ar-Fr₁₂ runs, respectively. These temperature gradients were the primary cause for the increased zero shifts of the high pressure injection gas tests relative to the low pressure injection gas tests. The axial force decreased throughout the cold air and hot air injection gas tests as illustrated in Figures 20 and 21, respectively. As the total temperature (T_t in Figures 20 and 21) increased, the balance thermal effects were more pronounced. Unlike the cold and hot air injection tests, the axial force did not stabilize for the Ar-Fr₁₂ injection tests (see Figure 22). This was a direct result of the inability of the injection gas controller to reach the desired plenum stagnation pressure (20 psia). So, the thrust oscillations produced by the injection gas caused the axial force measurements to oscillate. As

shown in Figures 20, 21, and 22, the plenum stagnation pressure (P_{ij}) oscillations were in phase with the axial force oscillations. Since the plenum pressure must stabilize before the forces and moments can be measured, the run time for injection gas tests is highly dependent upon the ability of the injection gas controller to reach the desired plenum stagnation pressure. For the injection tests of this investigation, the settling time of the plenum stagnation pressure ranged from 20 to 80 seconds. This was not an adequate controller for injection gas tests. Since the axial force shifts increase as the test progresses, a controller with sufficient damping is highly desirable to minimize the runtime when balance thermal effects are a major concern. The overshoot and settling time for the plenum stagnation pressure can be minimized if the proper damping is applied by the controller. Similar to the runs without gas injection, accurate axial force measurements can be obtained at the beginning of the injection gas tests. Unfortunately, a time span for accurate (less than 1 % of full scale) axial force measurements could not be defined due to oscillations in the axial force measurements at the beginning of these tests. However, the balance temperatures began increasing 10 seconds after model injection for the cold air injection tests. This suggests that accurate AF measurements can be obtained up to at least 10 seconds after model injection. Similarly, accurate AF measurements can be obtained within 5 seconds after model injection for the hot air and Ar-Fr₁₂ injection tests.

6 CONCLUSIONS

The thermal effects of gas injection and aerodynamic heating on the measurements of balance 2042 were evaluated. The normal force, side force, yaw moment, roll moment, and pitching moment balance measurements were unaffected by the balance heating effects of gas injection and wind tunnel flow. In general, the zero shifts of these components were less than the balance sensitivity (.5% of full scale). However, the axial force (AF) measurements of balance 2042 were significantly affected by balance heating. For the highest aerodynamic heating ($Re = 7 \times 10^6/ft$) without gas injection, the axial force shifts ranged from 1.8% to 4.2% during the tests. For these tests, the axial force measurements were accurate (less than 1% shift) up to 20 seconds after the model was injected into the test section. For cold air, hot air, and Ar-Fr₁₂ injection, the average AF shifts were 1.9%, 3.8%, and 5.9%, respectively. Possibly the AF shifts could have been reduced by calibrating the forward and aft sections of the axial force bridge circuit separately. During cold air injection, the AF measurements were accurate up to at least 10 seconds after model injection. The AF measurements were accurate up to at least 5 seconds after model injection for the hot air and Ar-Fr₁₂ injection tests. Since the plenum pressure must stabilize before the forces and moments can be measured, the runtime for injection gas tests is highly dependent upon the ability of the injection gas controller to reach the desired plenum stagnation pressure. Therefore, a controller with sufficient damping is highly desirable to minimize the runtime when balance thermal effects are a concern.

Within the scope of this investigation, non-watercooled, flow-through balances are not practical for scramjet exhaust flow simulation tests. Without watercooling, flow through balances will not provide accurate axial force measurements except at the beginning of the test, and the time span for accurate axial force measurements is highly restrictive. Even if an adequate plenum pressure controller is available for the injection gas system of the facility, during hot air and Ar-Fr₁₂ injection, the time span is only sufficient enough to evaluate one condition (i.e. AOA, plenum pressure) for the vehicle. Unlike typical force and moment tests where an entire angle of attack sweep is evaluated for each test. Also, several hours must be allowed between each test for the model and balance to cool properly. Approximately one hour was necessary for the HAPCM-50 and balance 2042 to cool down. In conclusion, the author recommends further investigation into watercooling flow-through balances.

7 REFERENCES

1. Hartill, William R., "Method for Obtaining Aerodynamic Data on Hypersonic Configurations with Scramjet Exhaust Flow Simulation", Rockwell International, Los Angeles Aircraft Division, Report No. NA-76-752, Los Angeles, Ca. June 1977.
2. Oman, R. A.; Foreman, K. M.; Leng, J.; and Hopkins, M. B., "Simulation of Hypersonic Scramjet Exhaust", NASA CR-2494, March 1975.
3. Miller, C.G. and Smith, F.M., "Langley Hypersonic Facilities and Complex Description", AIAA Paper No. 86-0741-CP, March 1986.
4. Holman, H.P., Experimental Methods for Engineers, New York: McGraw-Hill Book Company, 1989.
5. Cabbage, James M. and Monta, William J., "A Parametric Experimental Investigation of a Scramjet Nozzle Using Cold Gas Exhaust Simulation", proposed NASA TP No. 505-61-71-01, 1990
6. Newsome, R. W.; Walters, R. W.; Thomas, J. L., "An Efficient Iteration Strategy for Upwind/Relaxation Solutions to the Thin-Layer Navier-Stokes Equations", AIAA Paper 87-1113, June 1987.
7. Thomas, J. L. and Walters R. W., "Upwind Relaxation Algorithms for Navier-Stokes Equations", AIAA Journal, Vol. 25, April 1987, pp. 527-534.
8. Vigneron, Y. C.; Rakich, J. V.; and Tannehill, J. C., "Calculation of Supersonic Viscous Flow Over Delta Wings and Sharp Subsonic Leading Edges", AIAA Paper 78-1137, July 1978.
9. Eriksson, L. E., "Practical Three-Dimensional Mesh generation Using Transfinite Interpolation", SIAM Journal on Scientific and Statistical computing, Vol 6, July 1985, pp. 712-741.

TABLE I
Computational Solutions

| Re (x10 /ft) | AOA (deg) | C _{ac} | C _{ae} | % Diff (Ca) | C _{nc} | C _{ne} | % Diff (Cn) |
|-----------------|--------------|-----------------|-----------------|-------------|-----------------|-----------------|-------------|
| .5 | -3.5 | .0858 | .0412 | 52.0 | -.1229 | -.1248 | 1.5 |
| .5 | 0 | .0610 | .1286 | 110.8 | .0174 | .0325 | 86.8 |
| .5 | 5 | .0944 | .1131 | 19.8 | .2705 | .2842 | 5.1 |
| 1 | 0 | .0688 | .1388 | 101.7 | .0178 | .0123 | 30.9 |
| 2 | -3.5 | .0801 | .0548 | 31.6 | -.1548 | -.1271 | 17.9 |
| 2 | 0 | .0600 | .1112 | 46.0 | .0178 | .0229 | 28.7 |
| 2 | 5 | .0902 | .124 | 27.0 | .2739 | .2772 | 1.2 |
| 4 | 0 | .0732 | .0944 | 29.0 | .0166 | .0078 | 53.0 |
| 7 | -3.5 | .0650 | .0629 | 3.2 | -.1235 | -.1303 | 5.5 |
| 7 | 0 | .0643 | .1066 | 65.8 | .0167 | .0081 | 51.5 |
| 7 | 5 | .0706 | .1022 | 30.9 | .2749 | .2894 | 5.3 |

NOTE: % Diff = $\left| \frac{\text{experimental} - \text{computational}}{\text{computational}} \right| \times 100\%$

TABLE 2
Test Matrix

| Model | Re (x10 /ft) | Po (psia) | To (deg F) | AOA (deg) | Ptj (psia) | Ttj (deg F) |
|----------------------------|-----------------|--------------|---------------|--------------|---------------|----------------|
| Unpowered Configuration | .5 | 30 | 410 | -3.5 | -- | -- |
| | .5 | 30 | 410 | 0 | -- | -- |
| | .5 | 30 | 410 | 5 | -- | -- |
| | 1 | 60 | 410 | 0 | -- | -- |
| | 2 | 125 | 450 | -3.5 | -- | -- |
| | 2 | 125 | 450 | 0 | -- | -- |
| | 2 | 125 | 450 | 5 | -- | -- |
| | 4 | 250 | 450 | 0 | -- | -- |
| | 7 | 475 | 475 | -3.5 | -- | -- |
| | 7 | 475 | 475 | 0 | -- | -- |
| | 7 | 475 | 475 | 5 | -- | -- |
| Powered Configuration | .5 | 30 | 410 | 0 | -- | -- |
| | .5 | 30 | 410 | 5 | -- | -- |
| | 7 | 475 | 475 | 0 | -- | -- |
| | 7 | 475 | 475 | 5 | -- | -- |
| Cold Air Injection | .5 | 30 | 410 | 0 | 20 | 200 |
| | .5 | 30 | 410 | 5 | 20 | 200 |
| | 7 | 475 | 475 | 0 | 20 | 200 |
| | 7 | 475 | 475 | 5 | 20 | 200 |
| Hot Air Injection | .5 | 30 | 410 | 0 | 20 | 500 |
| | .5 | 30 | 410 | 5 | 20 | 500 |
| | 7 | 475 | 475 | 0 | 20 | 500 |
| | 7 | 475 | 475 | 5 | 20 | 500 |
| Ar-Fr-12 Injection | .5 | 30 | 410 | 0 | 20 | 500 |
| | .5 | 30 | 410 | 5 | 20 | 500 |
| | 7 | 475 | 475 | 0 | 20 | 500 |
| | 7 | 475 | 475 | 5 | 20 | 500 |

TABLE 3
Balance 2042 Zero Shifts

| Model | Re (x10/ft) | AOA (deg) | AF Zero Shift (% of full scale) | PM Zero Shift (% of full scale) | NF Zero Shift (% of full Scale) |
|----------------------------|----------------|--------------|------------------------------------|------------------------------------|------------------------------------|
| Unpowered Configuration | .5 | -3.5 | 2.5 | 0.0 | .1 |
| | .5 | 0 | .6 | 0.0 | 0.0 |
| | .5 | 5 | .8 | 0.0 | 0.0 |
| | 1 | 0 | 2.7 | 0.0 | 0.0 |
| | 2 | -3.5 | 4.0 | 0.0 | .1 |
| | 2 | 0 | 1.8 | .1 | .2 |
| | 2 | 5 | 1.3 | 0.0 | .1 |
| | 4 | 0 | 3.0 | 0.0 | 0.0 |
| | 7 | -3.5 | 2.8 | 0.0 | 0.0 |
| | 7 | 0 | 11.5 | 0.0 | .2 |
| 7 | 5 | 2.5 | 0.0 | .1 | |
| Powered Configuration | .5 | 0 | 0.0 | 0.0 | .2 |
| | .5 | 5 | 1.5 | 0.0 | 0.0 |
| | 7 | 0 | * | * | * |
| | 7 | 5 | * | * | * |
| Cold Air Injection | .5 | 0 | 1.0 | 0.0 | .4 |
| | .5 | 5 | 1.6 | 3.0 | .1 |
| | 7 | 0 | 1.1 | 0.0 | .2 |
| | 7 | 5 | 3.8 | .5 | .2 |
| Hot Air Injection | .5 | 0 | 3.0 | 0.0 | .4 |
| | .5 | 5 | 3.8 | 0.0 | 0.0 |
| | 7 | 0 | 2.5 | 0.0 | .1 |
| | 7 | 5 | 5.8 | 0.0 | .2 |
| Ar-Fr-12 Injection | .5 | 0 | 4.9 | 0.0 | .1 |
| | .5 | 5 | 4.8 | 0.0 | 0.0 |
| | 7 | 0 | 8.2 | .5 | .1 |
| | 7 | 5 | 5.8 | .5 | .2 |

* Data Acquisition Problems

TABLE 4
Balance 2042 Axial Force Shifts

| Model | Re (x10 /ft) | AOA (deg) | Run time (sec) | AF Shift (wind on) (% of Full Scale) |
|----------------------------|-----------------|--------------|-------------------|---|
| Unpowered Configuration | .5 | -3.5 | 74 | .6 |
| | .5 | 0 | 80 | .3 |
| | .5 | 5 | 84 | .4 |
| | 1 | 0 | 78 | .5 |
| | 2 | -3.5 | 85 | 1.2 |
| | 2 | 0 | 35 | 1.4 |
| | 2 | 5 | 81 | 1.7 |
| | 4 | 0 | 111 | .3 |
| | 7 | -3.5 | 110 | 1.8 |
| | 7 | 0 | 107 | 4.2 |
| 7 | 5 | 111 | 2.8 | |
| Powered Configuration | .5 | 0 | 55 | .7 |
| | .5 | 5 | 90 | .4 |
| | 7 | 0 | 81 | * |
| | 7 | 5 | 70 | * |
| Cold Air Injection | .5 | 0 | 86 | AF shift during the injection runs cannot be established due to AF oscillations |
| | .5 | 5 | 80 | |
| | 7 | 0 | 79 | |
| | 7 | 5 | 85 | |
| Hot Air Injection | .5 | 0 | 90 | |
| | .5 | 5 | 90 | |
| | 7 | 0 | 90 | |
| | 7 | 5 | 110 | |
| Ar-Fr-12 Injection | .5 | 0 | 92 | |
| | .5 | 5 | 70 | |
| | 7 | 0 | 85 | |
| | 7 | 5 | 88 | |

* Data Acquisition Problems

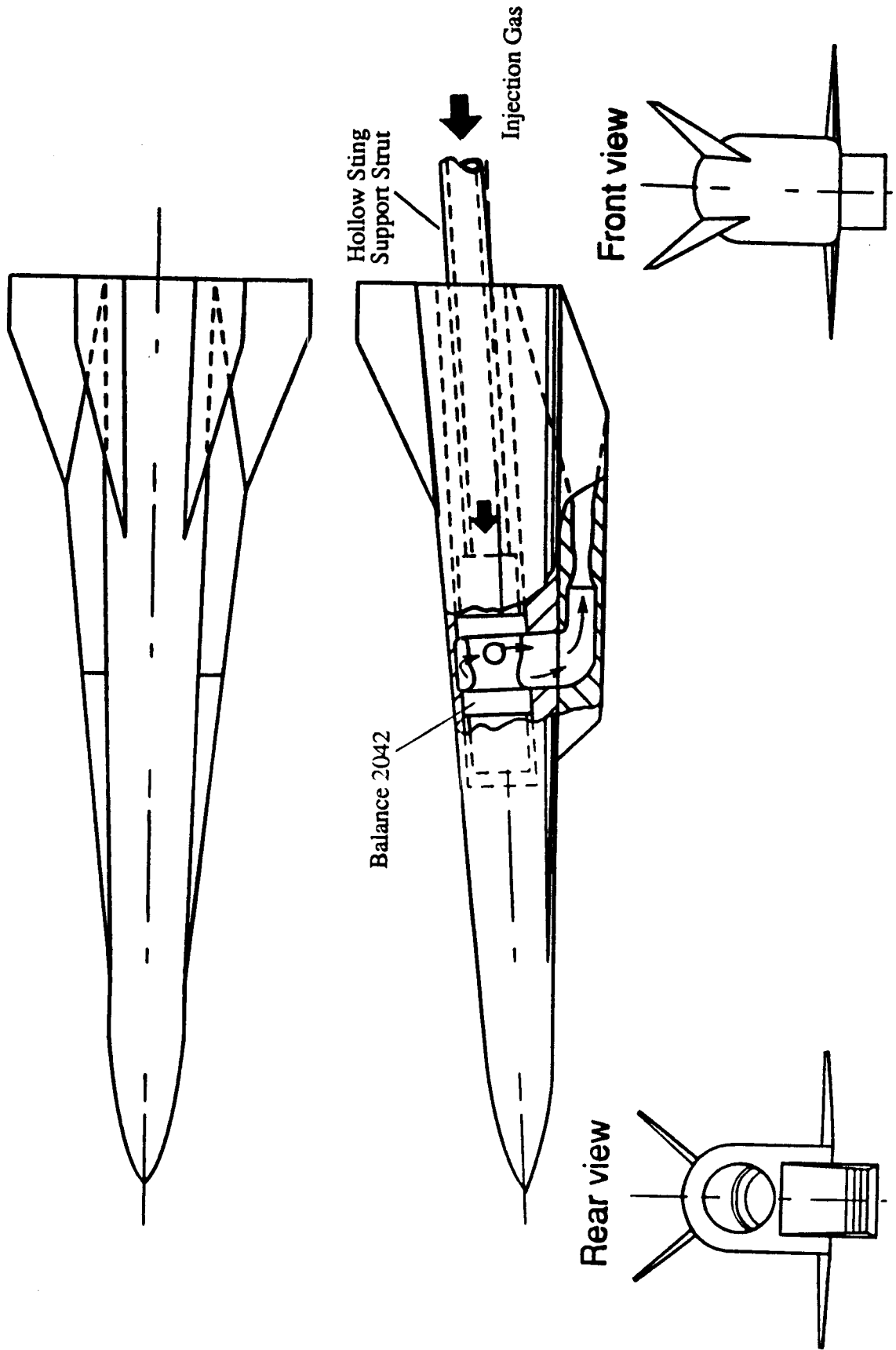
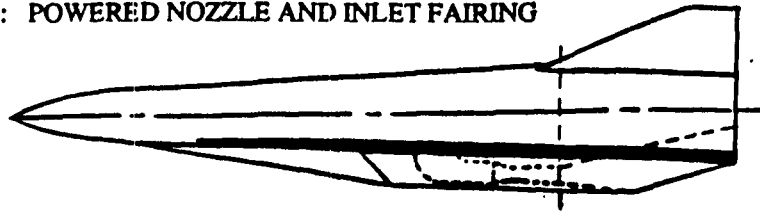


Figure 1: HAPCM-50 Internal Gas Injection

ADD AND SUBTRACT THE AERODYNAMIC FORCES/MOMENTS FOR THE FOLLOWING CONFIGURATIONS OF THE HAPCM-50 TO OBTAIN THE COMPLETE CONFIGURATION AERODYNAMIC FORCES/MOMENTS WITH AN OPERABLE INLET AND SCRAMJET ENGINE EXHAUST:

COMPLETE MODEL: POWERED NOZZLE AND INLET FAIRING

+



Combustor Exit

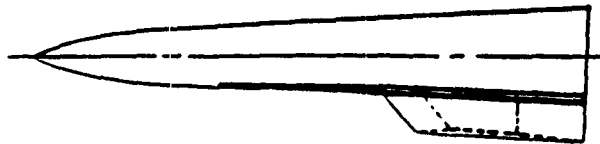
TRUNCATED MODEL: SHORT FLOW-THRU NACELLE AND INLET FAIRING

-



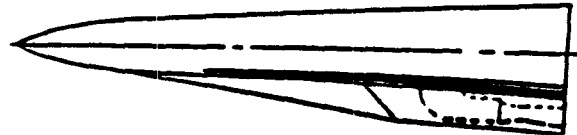
TRUNCATED MODEL: SHORT FLOW-THRU NACELLE

+



TRUNCATED MODEL: SHORT POWERED NOZZLE (NO TUNNEL FLOW)

-



COMPLETE CONFIGURATION WITH AN OPERABLE INLET AND SCRAMJET ENGINE EXHAUST

=

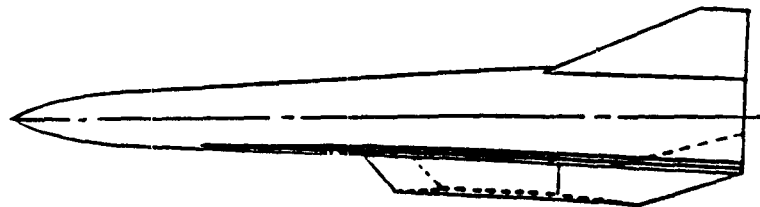
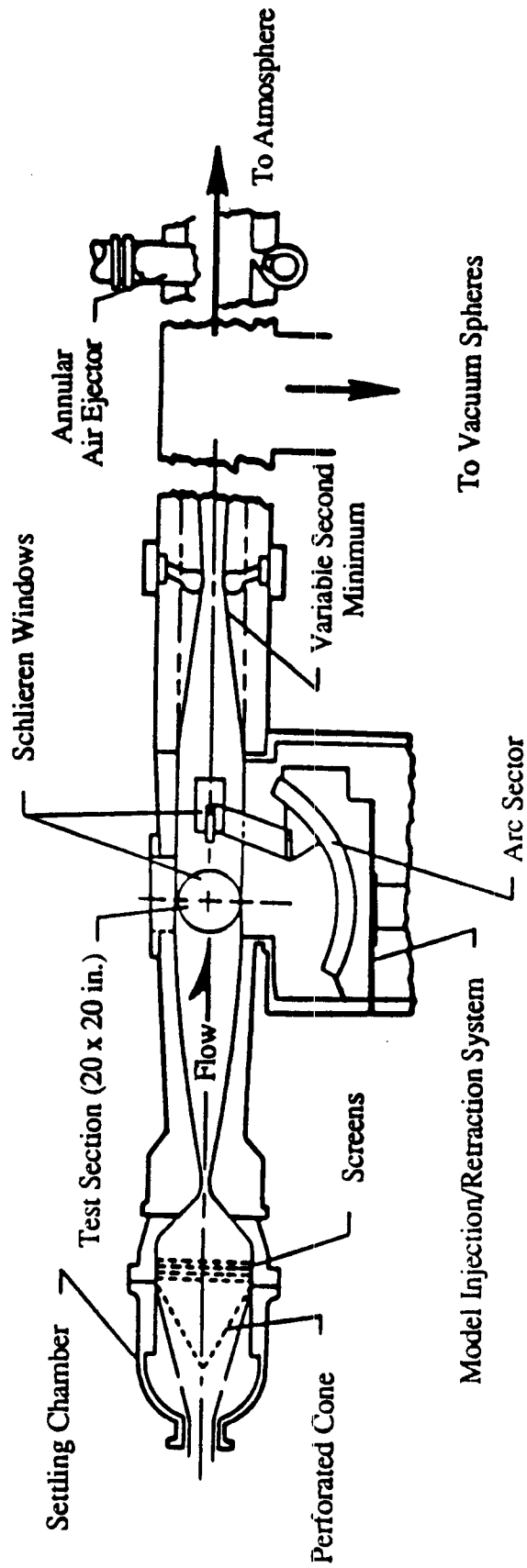


Figure 2: Force Accounting for the HAPCM-50.



| | |
|--|-------------|
| Mach Number | 6.0 |
| Reynolds Number (x 10 ⁶ per foot) | 0.5 to 10.5 |
| Total Pressure (psia) | 30 to 550 |
| Dynamic Pressure (psf) | 69 to 1264 |
| Total Temperature (deg R) | 810 to 1018 |
| Run Time (minutes) | up to 15 |

Figure 3: NASA Langley 20-Inch Mach 6 Wind Tunnel Schematic.

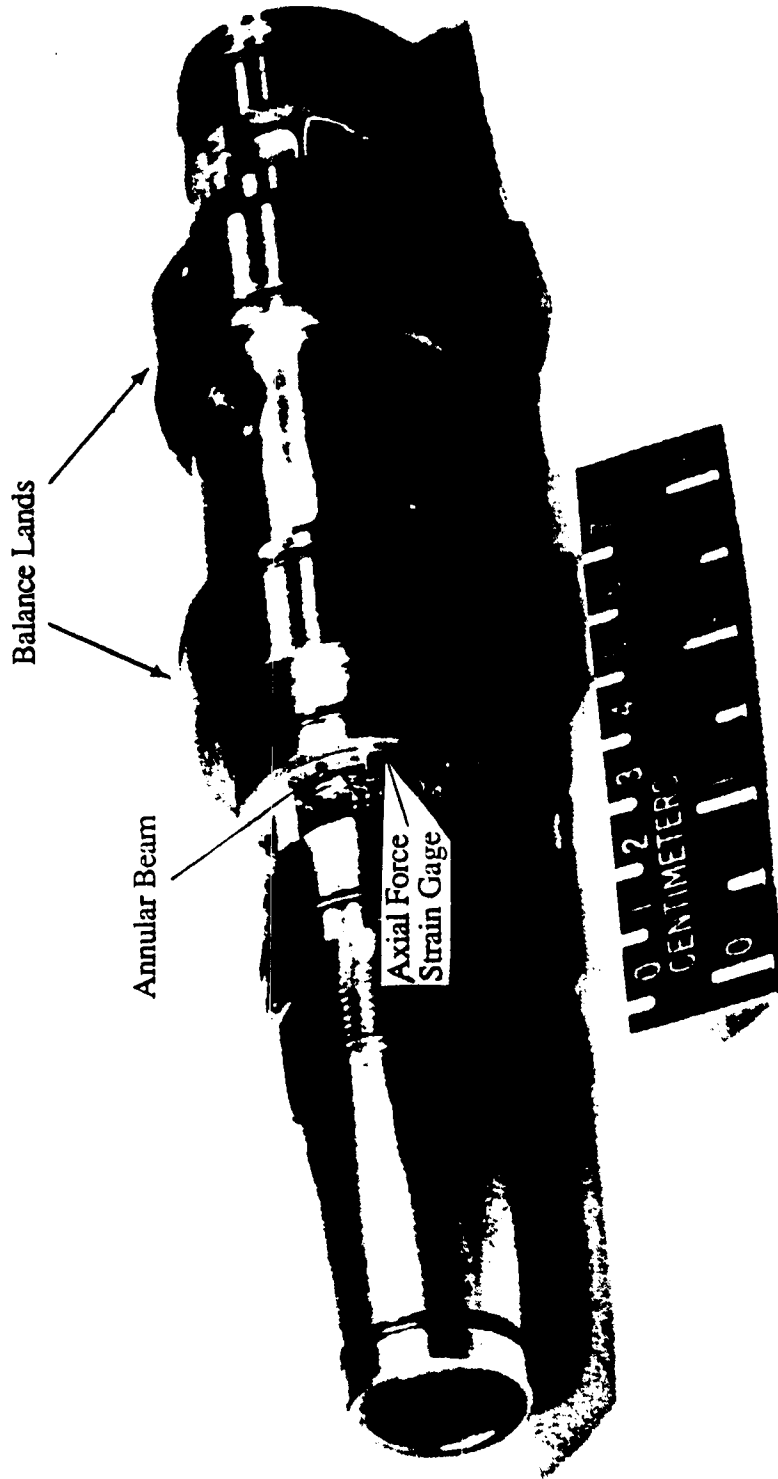
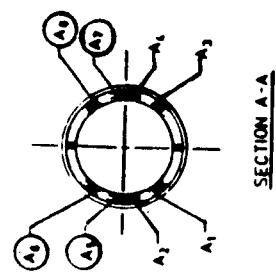
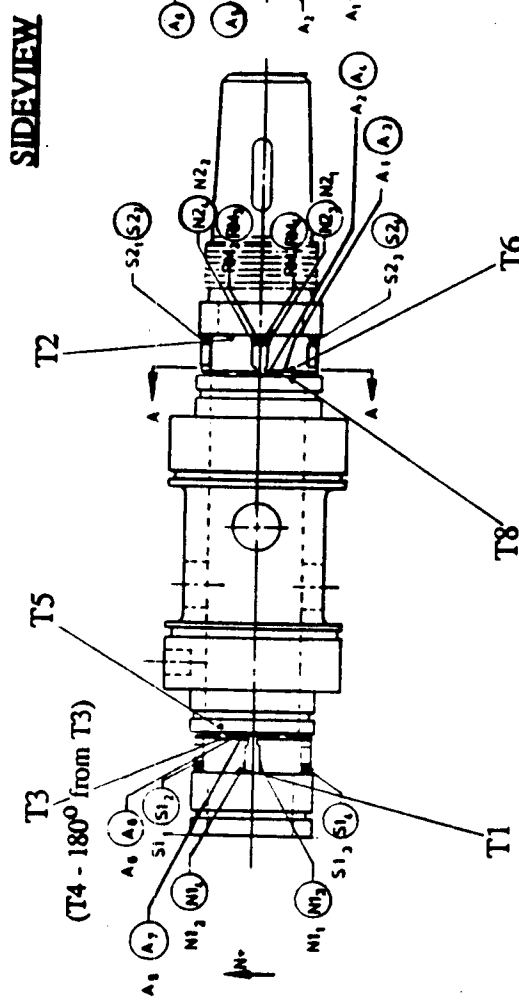
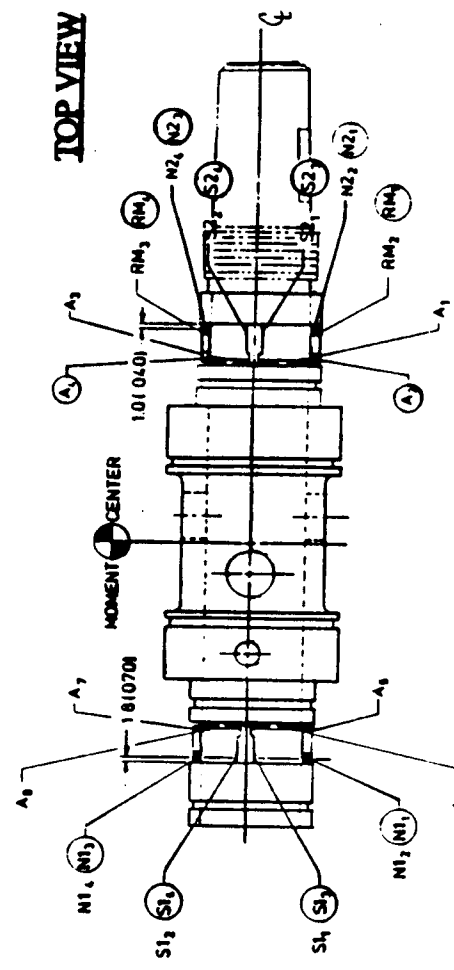
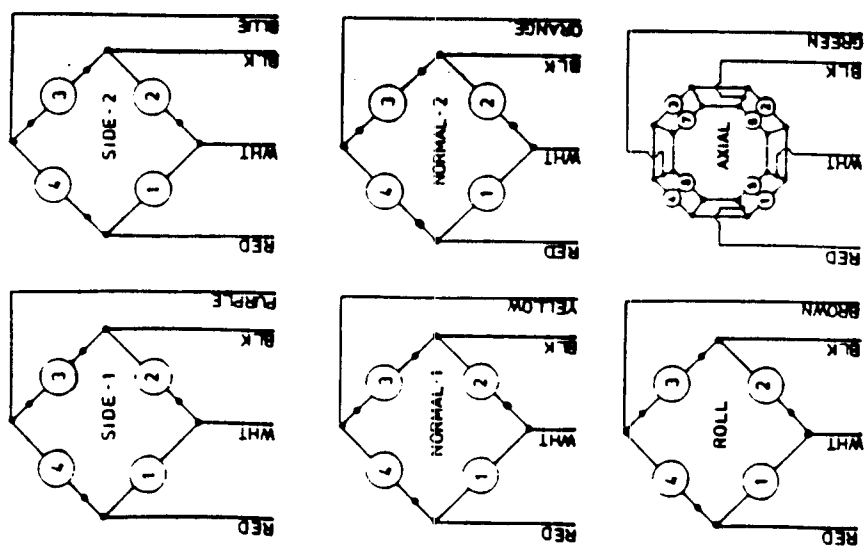
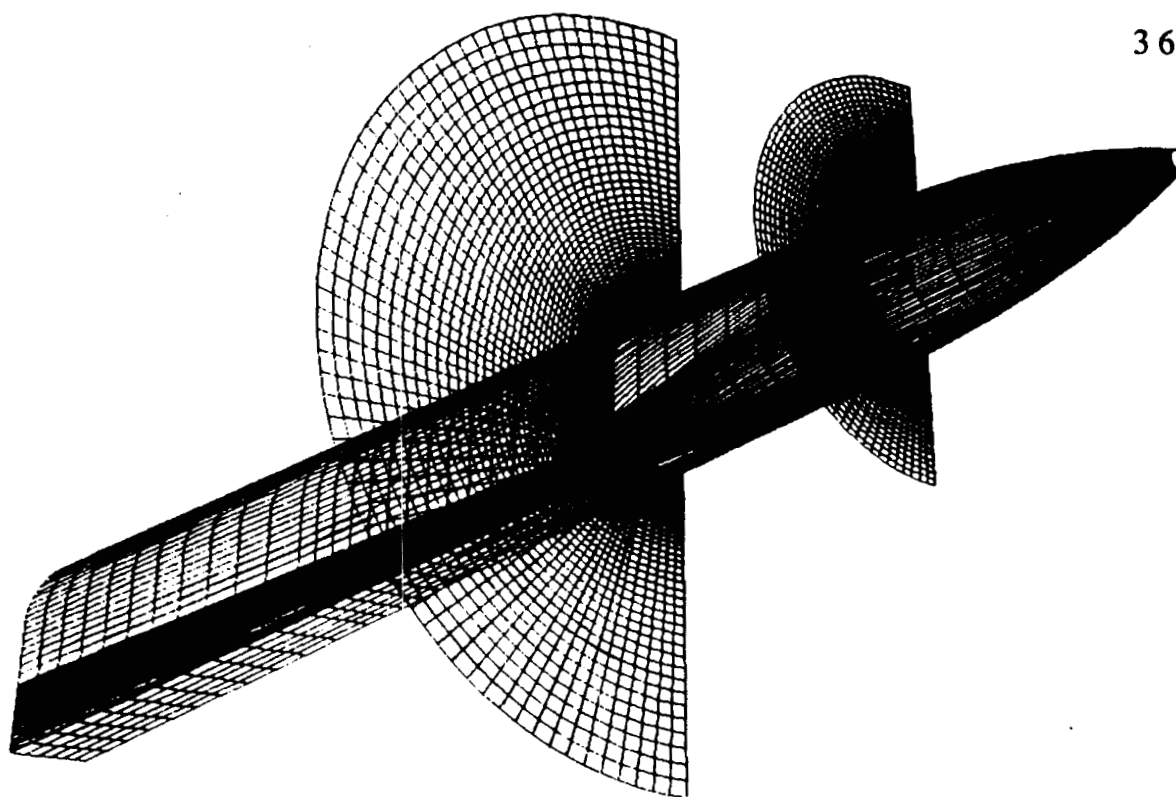


Figure 6: Annular Beams and Strain Gage Mounting in Balance 2042.



| LOAD CHART | | |
|------------|------------|--------------|
| COMPONENT | LBS | NEWTONS |
| NORMAL | 100 lbs | 444.82 N |
| AXIAL | 20 lbs | 88.964 N |
| PITCH | 200 in lbs | 22596.9 N mm |
| ROLL | 100 in lbs | 11298.5 N mm |
| YAW | 100 in lbs | 11298.5 N mm |
| SIDE | 50 lbs | 222.41 N |

Figure 7: Balance 2042 Strain-Gage Circuit Diagrams and Thermocouple Locations. 3 4



Typical Grid Cross-Flow Plane

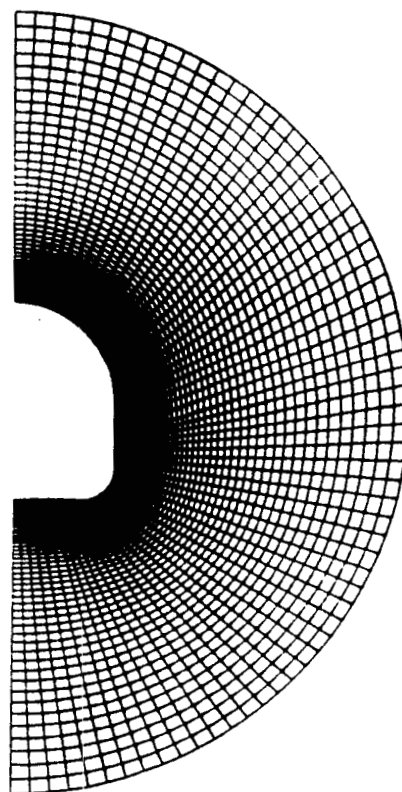


Figure 9: Computational Grid for Parabolized Navier-Stokes Solutions.

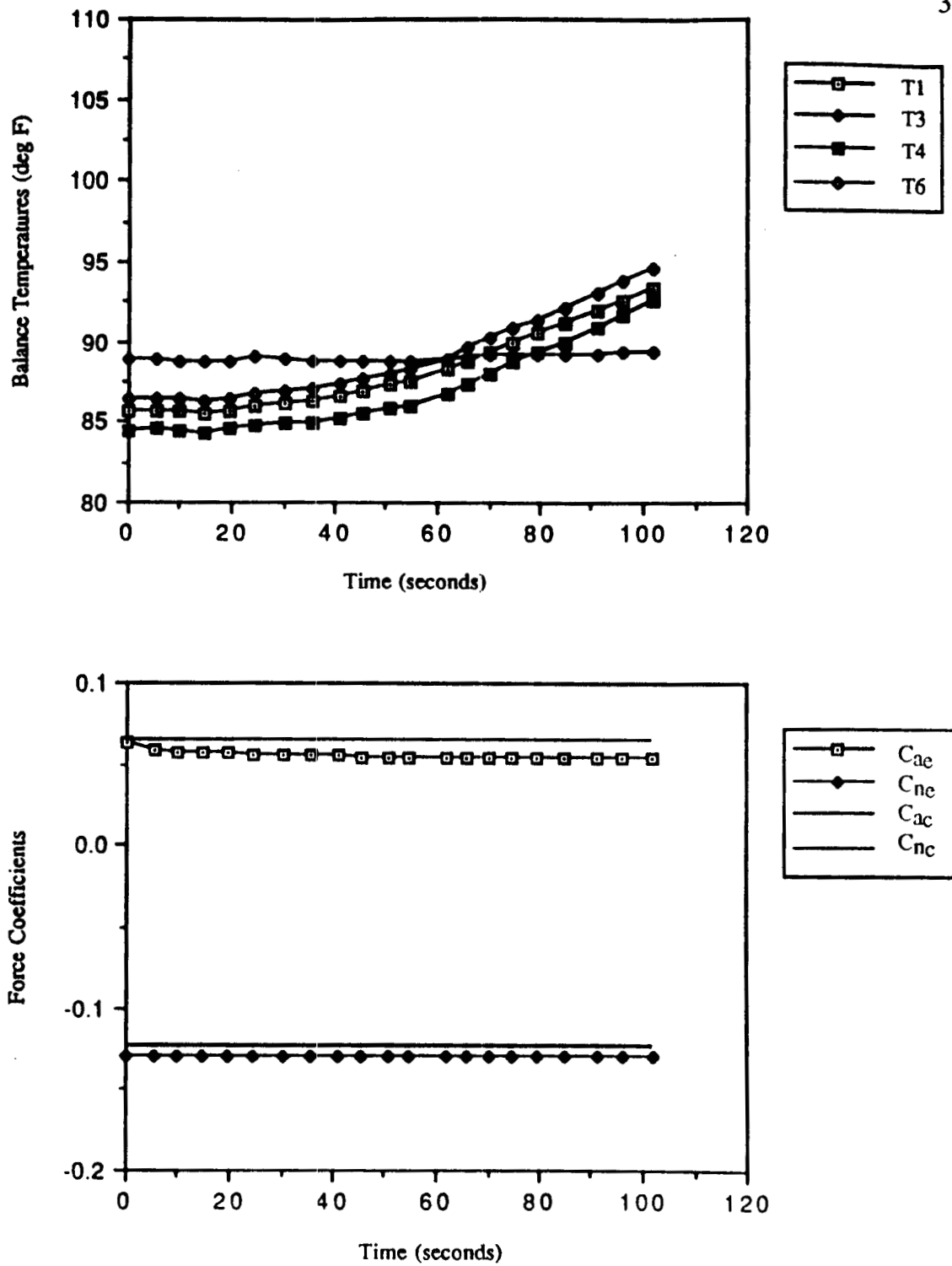


Figure 10: Computational Solution-Experimental Comparison For the Unpowered Configuration at -3.5 deg AOA with $Re=7 \times 10^6$ per foot and $M = 6$

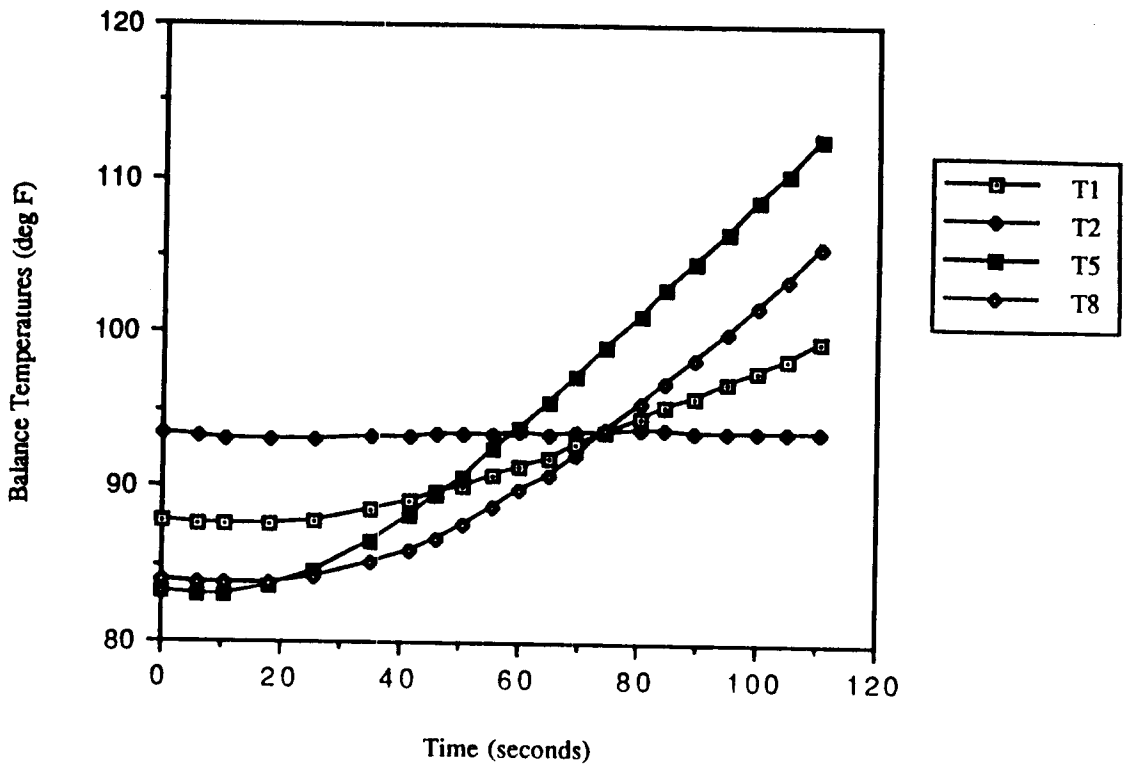


Figure 11: Balance Temperature Time Histories For the Unpowered Configuration at 5 deg AOA with $Re=7 \times 10^6$ per foot and $M = 6$

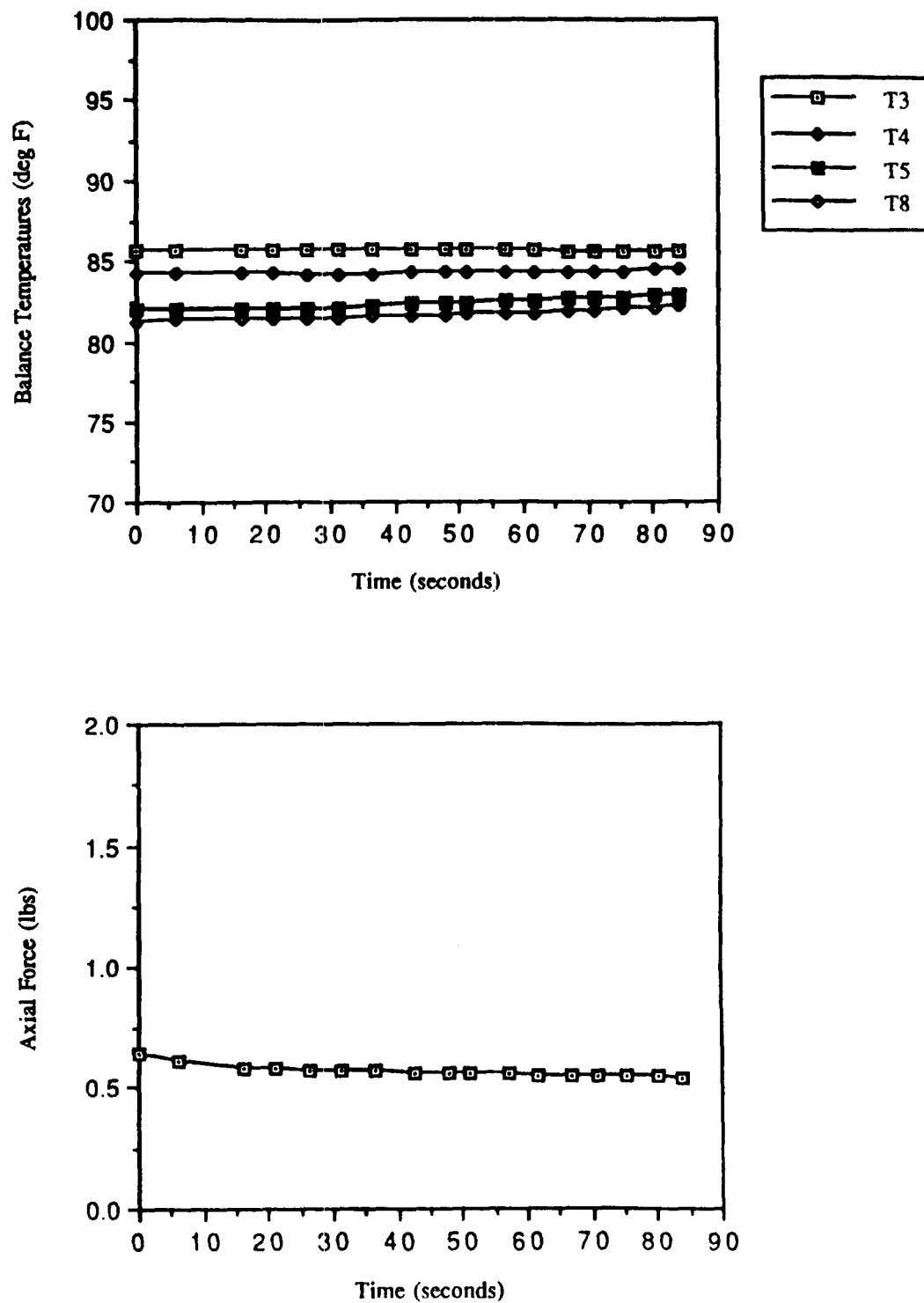


Figure 12: Axial Force and Balance Temperature Time Histories for the Unpowered Configuration at 5 deg AOA with $Re=0.5 \times 10^6/ft$ and $M=6$.

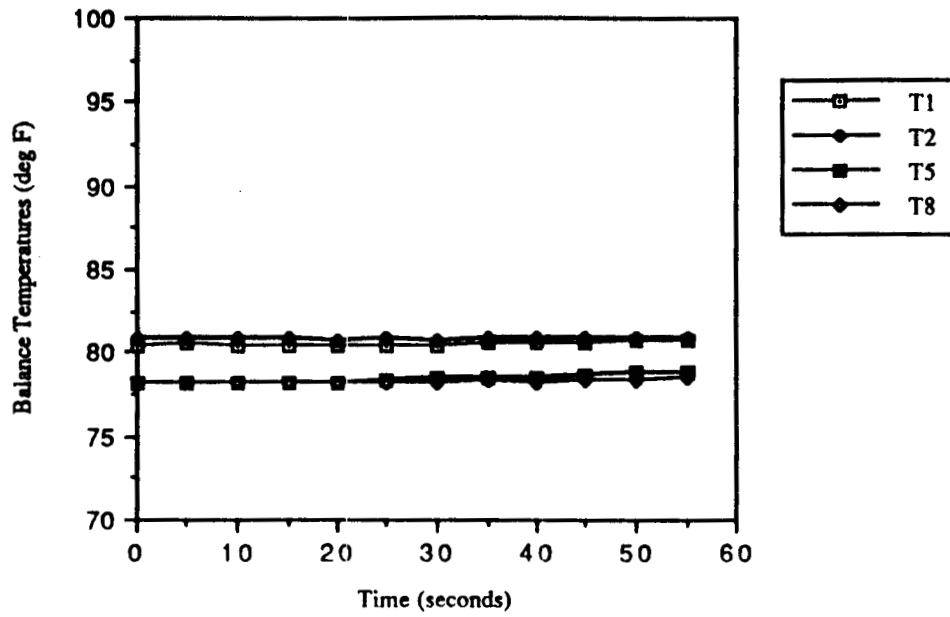


Figure 13: Balance Temperature Time Histories For the Powered Configuration at 0 deg AOA with $Re=.5 \times 10^6$ per foot and $M = 6$

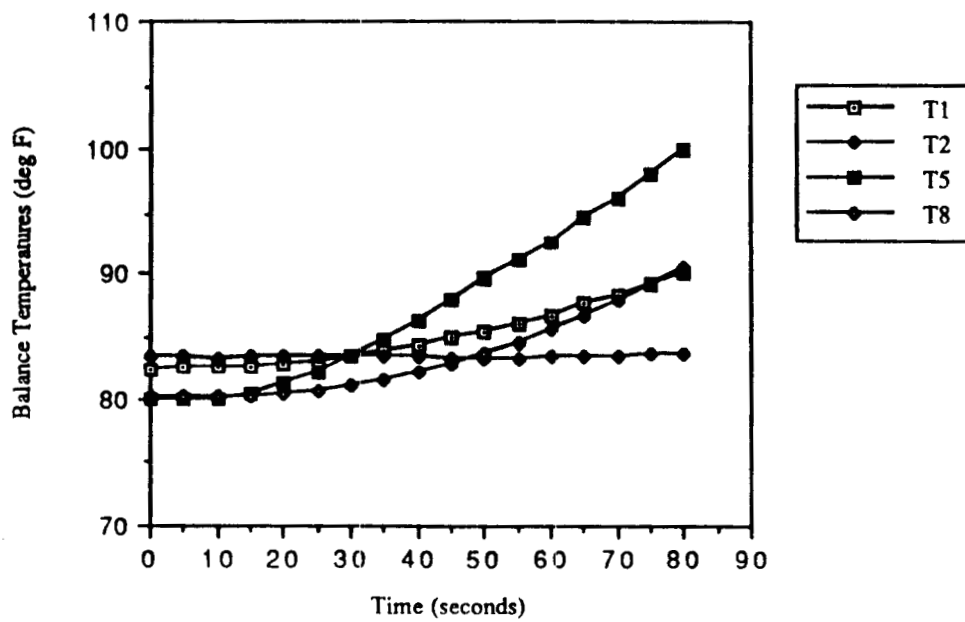


Figure 14: Balance Temperature Time Histories For the Powered Configuration at 0 deg AOA with $Re=7 \times 10^6$ per foot and $M = 6$

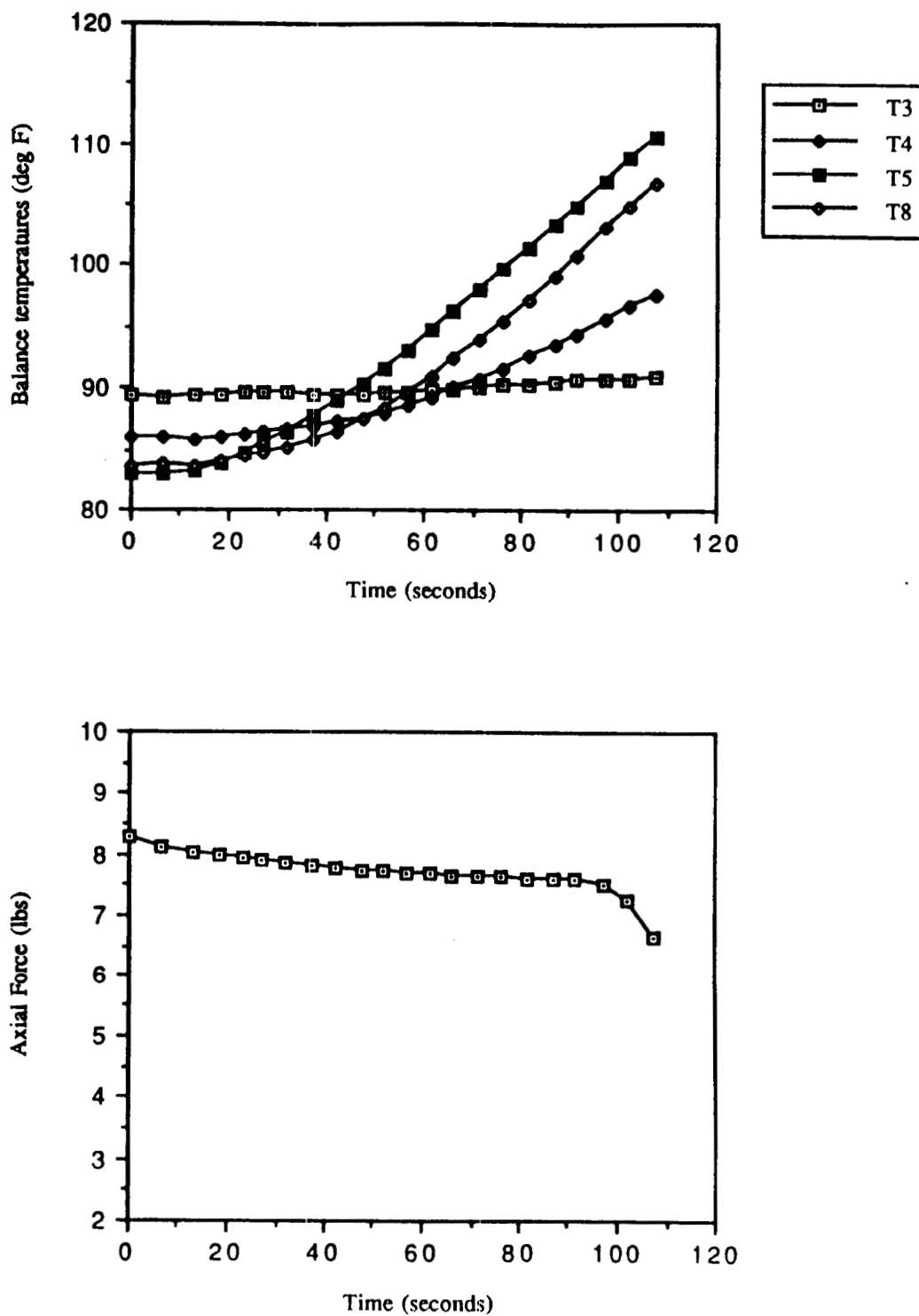


Figure 15: Axial Force and Balance Temperature Time Histories for the Unpowered Configuration at 0 deg AOA with $Re=7 \times 10^6/ft$ and $M=6$.

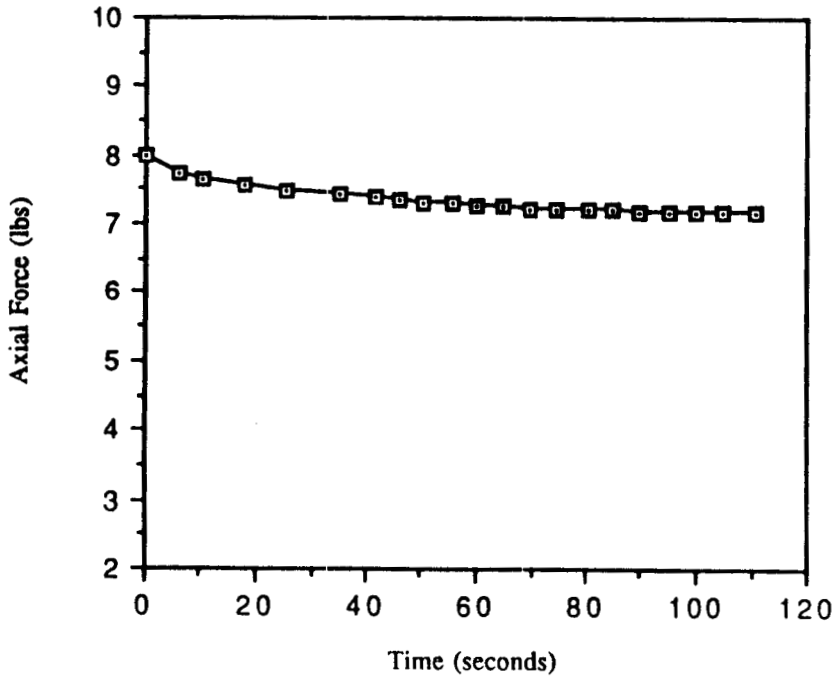
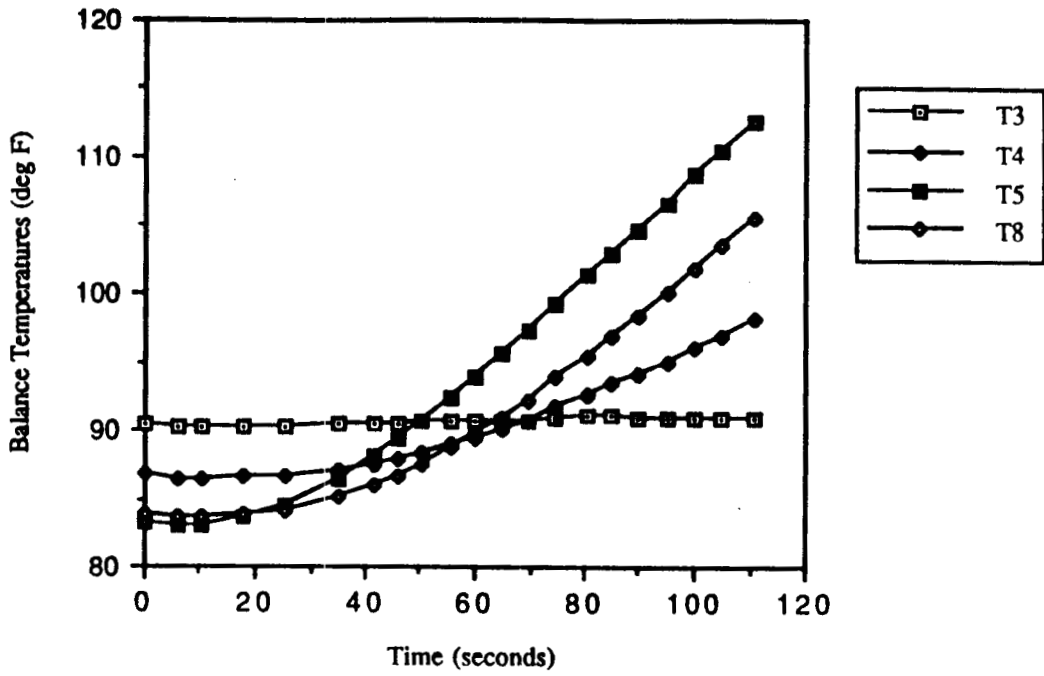


Figure 16: Axial Force and Balance Temperature Time Histories for the Unpowered Configuration at 5 deg AOA with $Re=7 \times 10^6/ft$ and $M=6$.

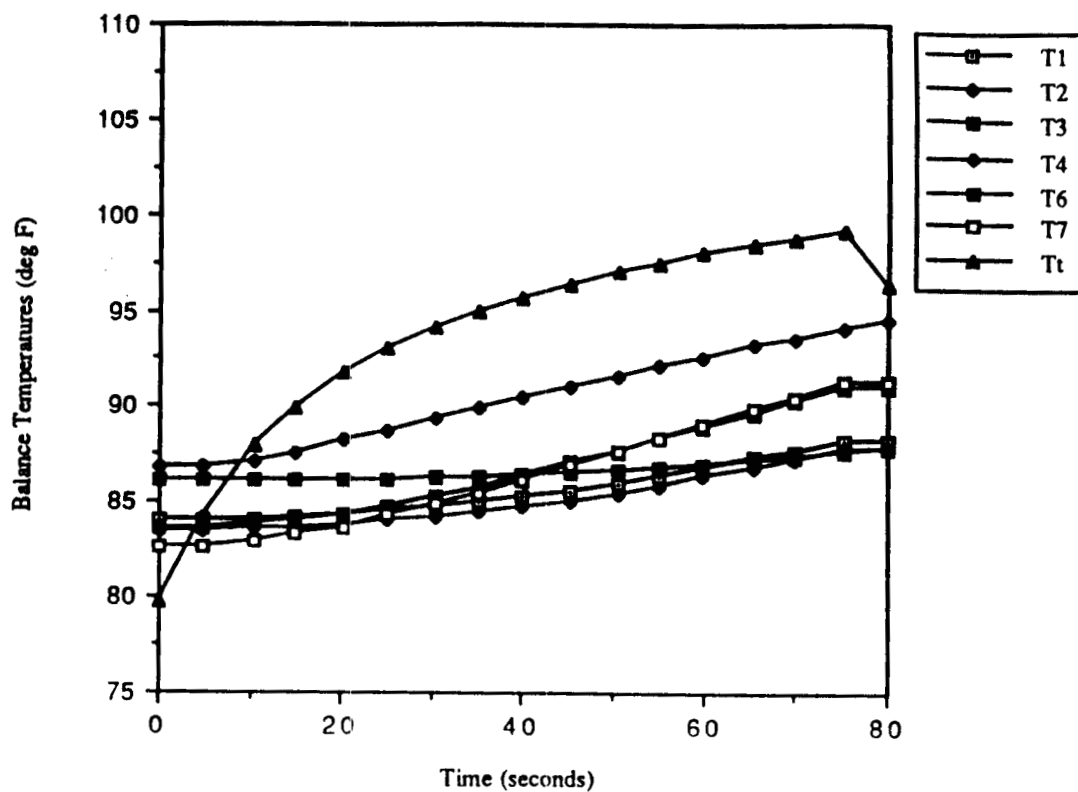


Figure 17: Balance Temperature Time Histories for the Powered Configuration at 5 deg AOA, $Re=0.5 \times 10^6/ft$, and $M=6$ with Cold Air Injection.

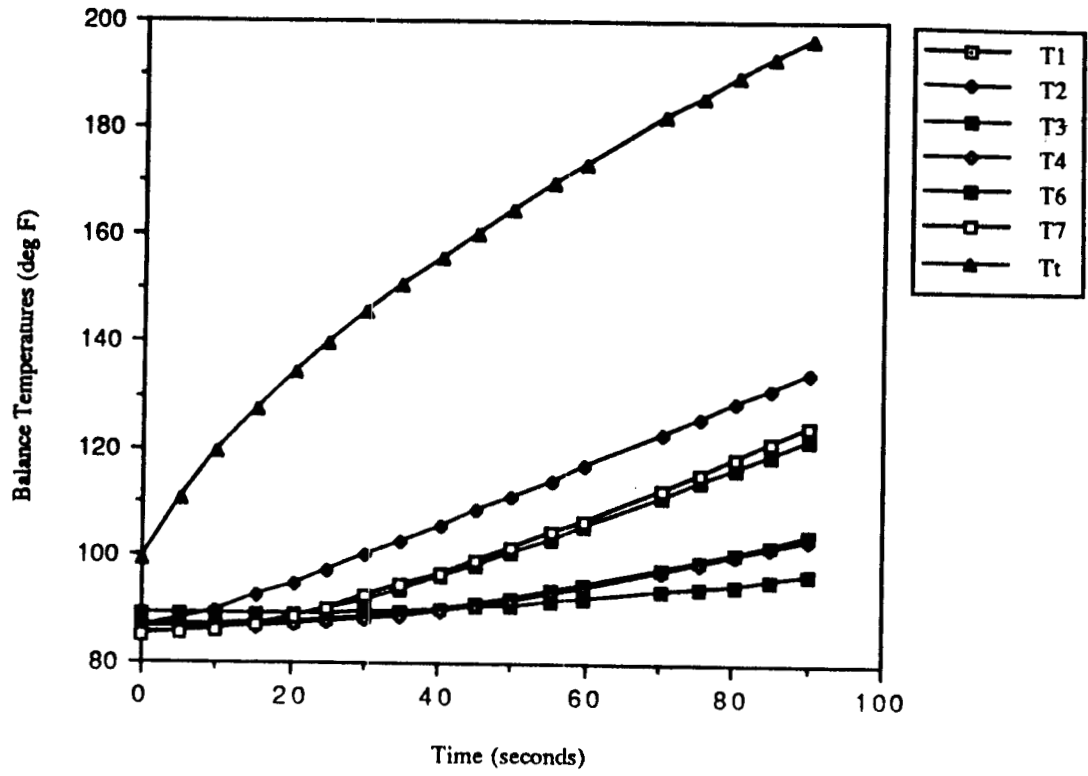


Figure 18: Balance Temperature Time Histories for the Powered Configuration at 5 deg AOA, $Re=0.5 \times 10^6/ft$, and $M=6$ with Hot Air Injection.

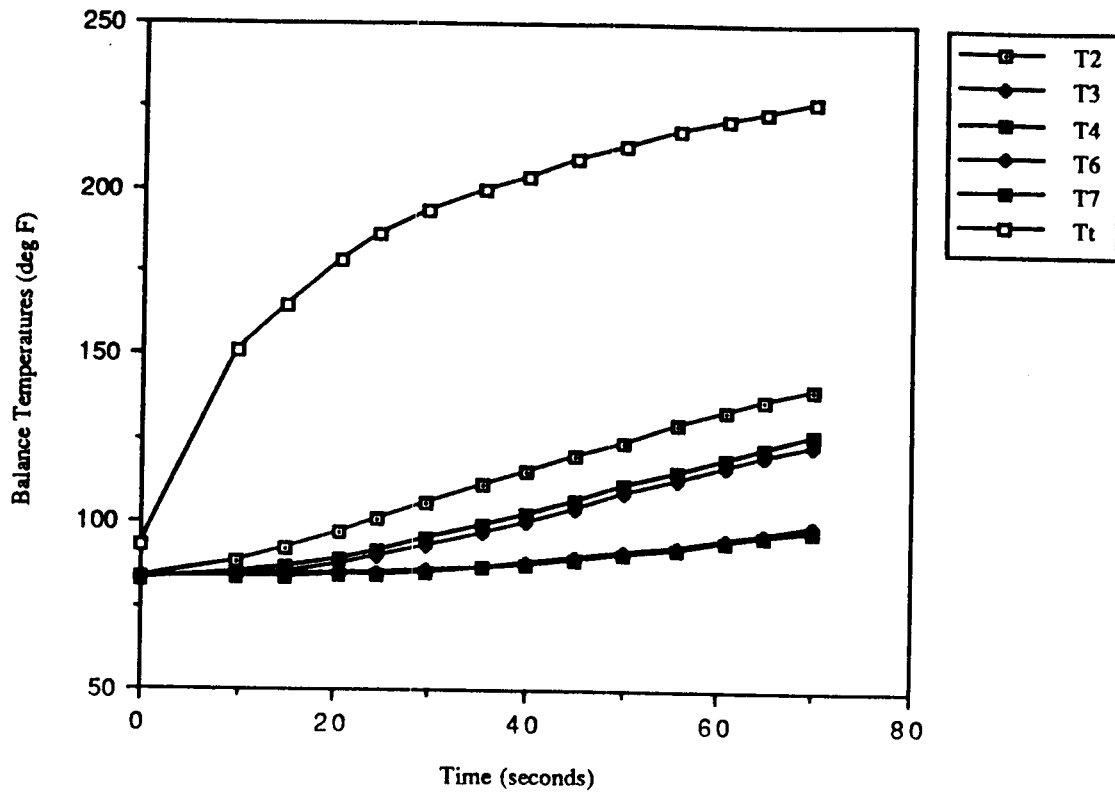


Figure 19: Balance Temperature Time Histories for the Powered Configuration at 5 deg AOA, $Re=0.5 \times 10^6/\text{ft}$, and $M=6$ with Ar- Fr_{12} Injection.

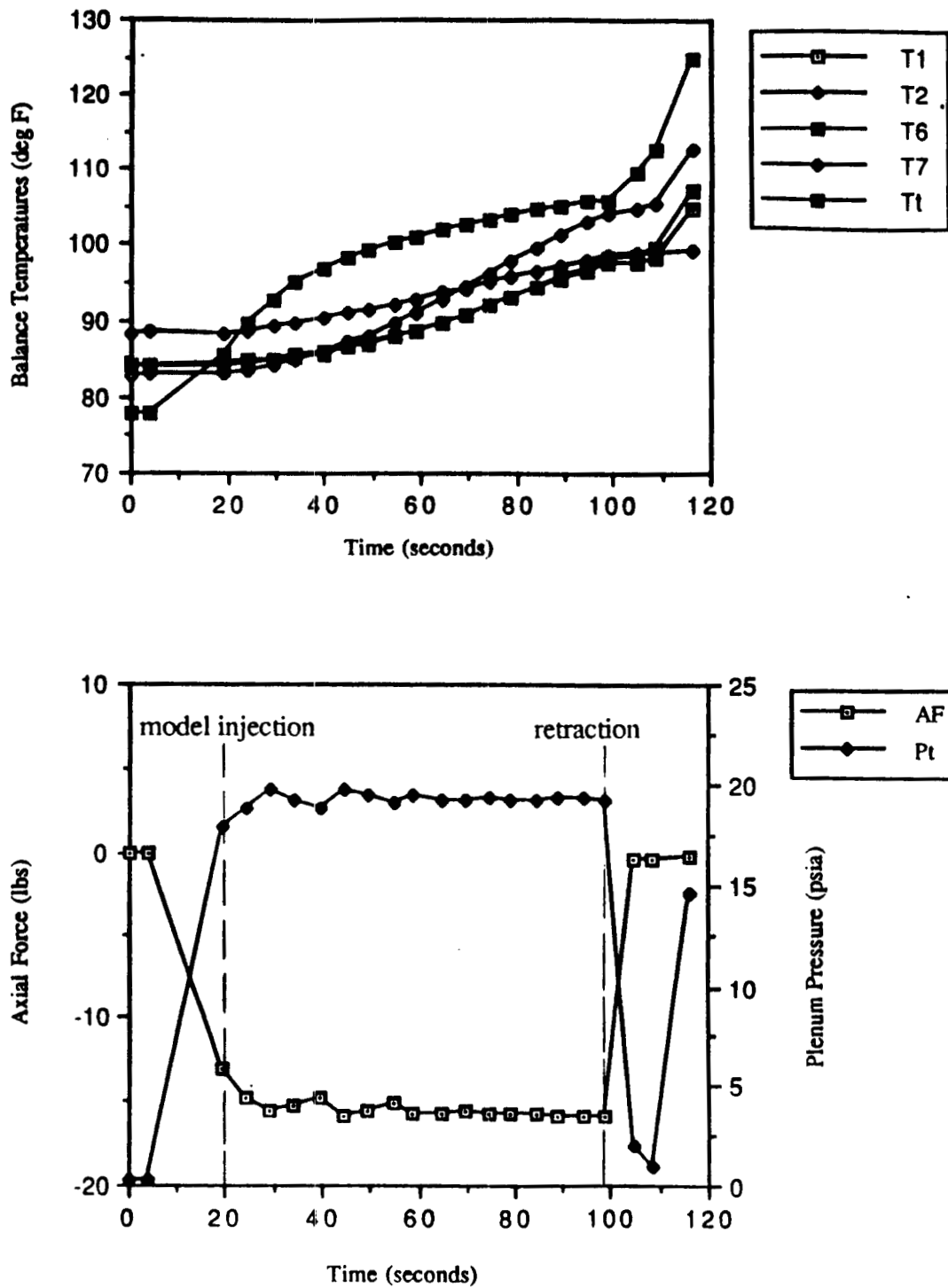


Figure 20: Axial Force and Balance Temperature Time Histories for the Powered Configuration at 0 deg AOA, $Re=7 \times 10^6/ft$ and $M=6$ with Cold Air Injection.

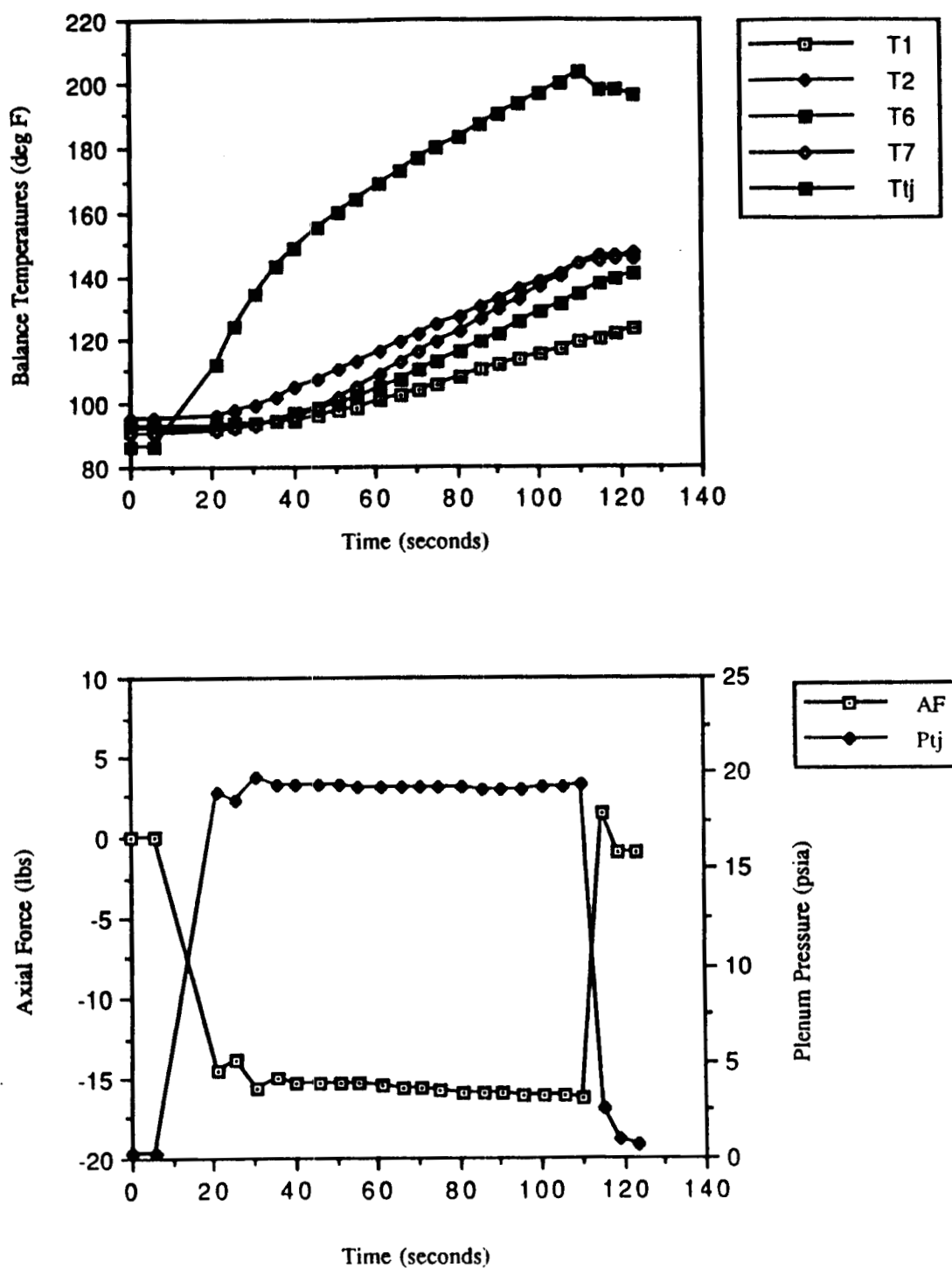


Figure 21: Axial Force and Balance Temperature Time Histories for the Powered Configuration at 0 deg AOA, $Re=7 \times 10^6/\text{ft}$ and $M=6$ with Hot Air Injection.

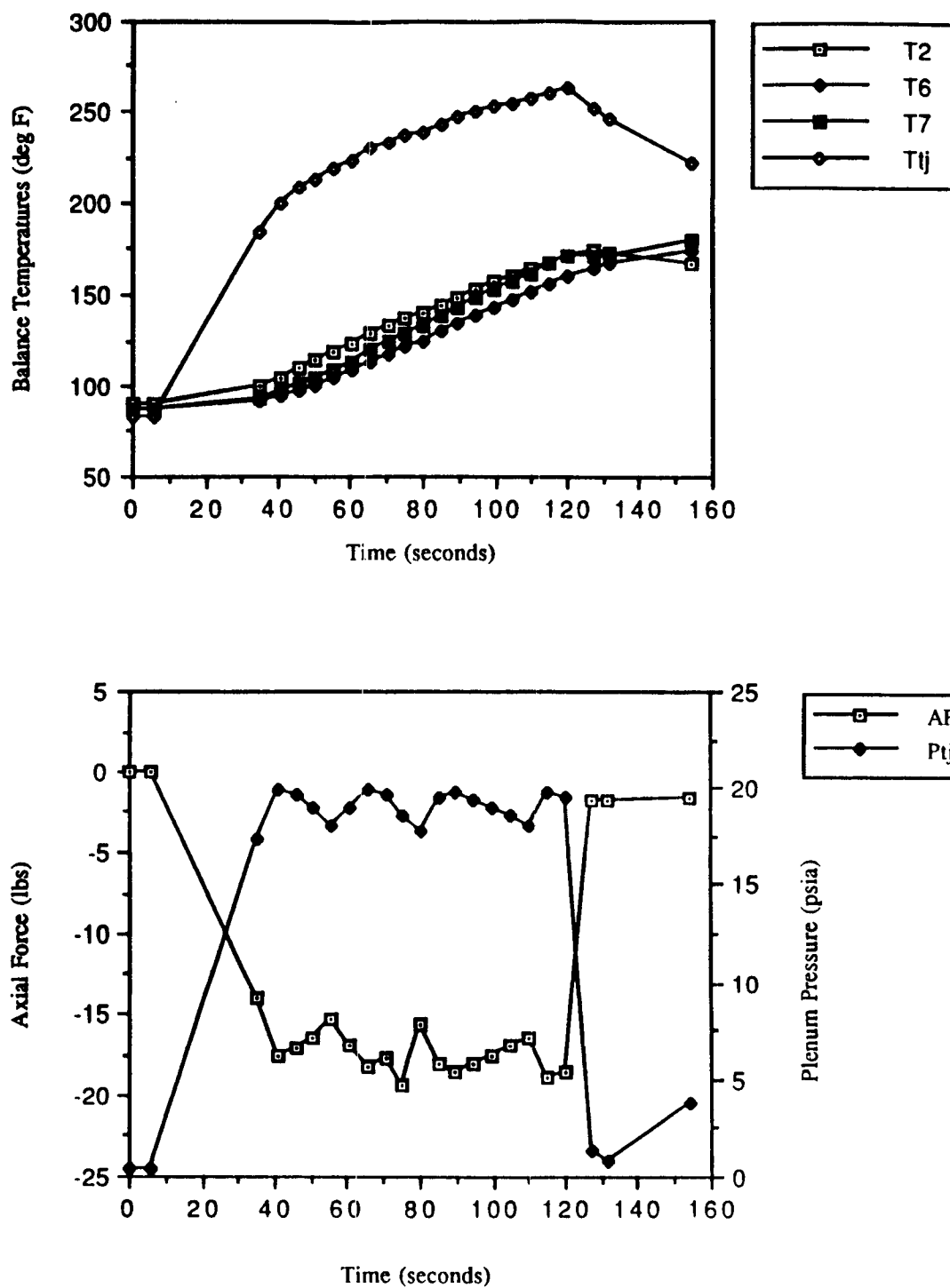


Figure 22: Axial Force and Balance Temperature Time Histories for the Powered Configuration at 0 deg AOA, $Re=7 \times 10^6/ft$ and $M=6$ with Ar-Fr₁₂ Injection.